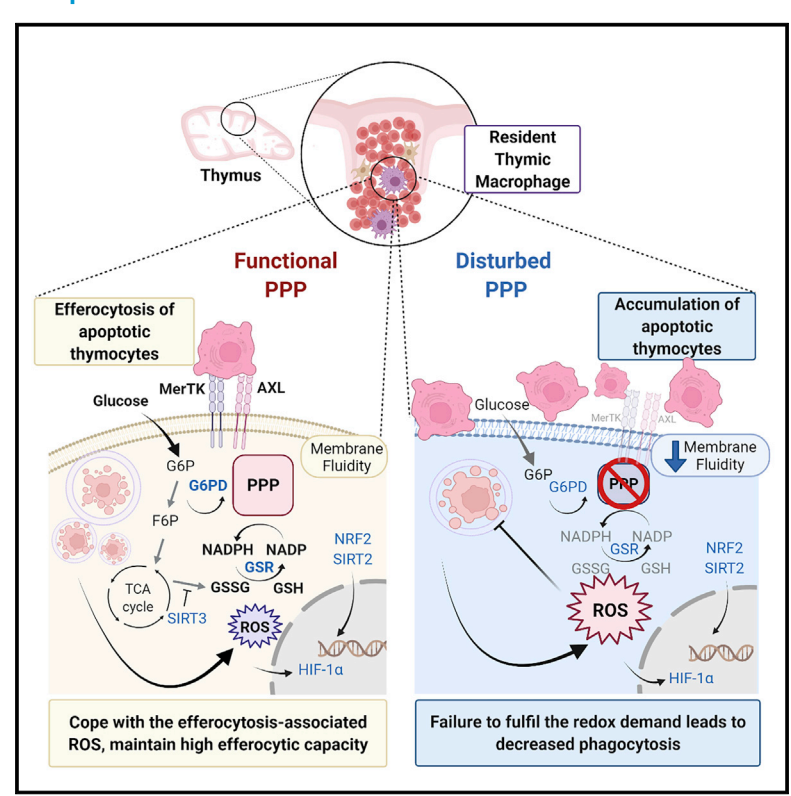
# Multiomics reveal the central role of pentose phosphate pathway in resident thymic macrophages to cope with efferocytosis-associated stress

### **Graphical abstract**



### **Authors**

Tsung-Lin Tsai, Tyng-An Zhou, Yu-Ting Hsieh, ..., Chih-Yu Lin, Ivan L. Dzhagalov, Chia-Lin Hsu

### Correspondence

clhsu@nycu.edu.tw

### In brief

Tsai et al. present multiomics analyses on the  $TM\phi s$  population and reveal that PPP is a crucial metabolic adaptation for  $TM\phi s$  to cope with oxidative stress and support efferocytosis. These results highlight the metabolic flexibility of TRMs and the multifaceted involvement of metabolic pathways in different biological settings.

### **Highlights**

- TMφs are a metabolically and transcriptionally distinct cell population
- The pentose phosphate pathway (PPP) is preferentially activated in TMφs
- PPP supports the reduction-oxidation demands associated with efferocytosis in TMφs
- Disturbance in PPP affects the efferocytosis efficiency







### **Article**

# Multiomics reveal the central role of pentose phosphate pathway in resident thymic macrophages to cope with efferocytosis-associated stress

Tsung-Lin Tsai, 1,5 Tyng-An Zhou, 1 Yu-Ting Hsieh, 1 Ju-Chu Wang, 1 Hui-Kuei Cheng, 1 Chen-Hua Huang, 2 Pei-Yuan Tsai, 1 Hsiu-Han Fan, 1 Hsing-Kai Feng, 1 Yu-Chia Huang, 1 Chen-Ching Lin, 3 Chao-Hsiung Lin, 2 Chih-Yu Lin, 4 Ivan L. Dzhagalov, 1 and Chia-Lin Hsu<sup>1,5,6,\*</sup>

#### **SUMMARY**

Tissue-resident macrophages (TRMs) are heterogeneous cell populations found throughout the body. Depending on their location, they perform diverse functions maintaining tissue homeostasis and providing immune surveillance. To survive and function within, TRMs adapt metabolically to the distinct microenvironments. However, little is known about the metabolic signatures of TRMs. The thymus provides a nurturing milieu for developing thymocytes yet efficiently removes those that fail the selection, relying on the resident thymic macrophages (TM $\phi$ s). This study harnesses multiomics analyses to characterize TM $\phi$ s and unveils their metabolic features. We find that the pentose phosphate pathway (PPP) is preferentially activated in TM $\phi$ s, responding to the reduction-oxidation demands associated with the efferocytosis of dying thymocytes. The blockade of PPP in M $\phi$ s leads to decreased efferocytosis, which can be rescued by reactive oxygen species (ROS) scavengers. Our study reveals the key role of the PPP in TM $\phi$ s and underscores the importance of metabolic adaptation in supporting M $\phi$  efferocytosis.

### **INTRODUCTION**

Tissue-resident macrophages (TRMs) are long-lived cells that exist in distinct microenvironments throughout the body. The niches they reside provide cues such as nutrient and cytokine availability, the type of cells they phagocytose, the anchoring scaffold they interact with, or the length of residency, which together define the identity and function of TRMs (Blériot et al., 2020; Gosselin et al., 2014; Guilliams and Svedberg, 2021; Guilliams et al., 2020; Zago et al., 2021). For example, interleukin (IL)-34 and transforming growth factor beta (TGF-β) are produced and maintained locally in the brain to support microglia survival and identity (Bohlen et al., 2017; Wang et al., 2012). Splenic red pulp macrophages are continuously exposed to heme generated from erythrocyte degradation, which drives their differentiation (Haldar et al., 2014). These findings highlight the intimate crosstalk between the microenvironment and TRM specification. While genes serve as the blueprints for an organism's biological functions, their expression is closely intertwined with environmental cues. As a result, it is becoming clear that metabolism influences and is influenced by gene expression as well. The metabolic interplay between the microenvironment

and TRMs is just starting to be identified. The contribution of microenvironment-enriched metabolites in TRM imprinting is demonstrated by retinoic acid, the peritoneal cavity enriched metabolite that induces the expression of Gata6 for lineage specification of peritoneal cavity macrophages (PCM $\phi$ s) (Gautier et al., 2014; Okabe and Medzhitov, 2014). When encountering microbe challenges, the PCM $\phi$ s are metabolically poised to utilize glutamate, another locally abundant metabolite, to fuel the inflammatory responses (Davies et al., 2017). Different tissues have a broad spectrum of metabolic rates (Wang et al., 2010) and metabolite compositions (Jang et al., 2019), raising interesting questions about how TRMs can metabolically adapt to and function within distinct microenvironments.

Thymopoiesis, the continual supply of the diverse yet tolerant T cells, relies on the thymus to provide the selective but nurturing harbor for developing thymocytes. The thymus is separated from the circulation to avoid unselected developing thymocytes being in contact with the peripheral tissues, at the expense of low nutrient and oxygen availability (Ribatti, 2015). As a dynamic and competitive process, it is estimated that 95% of newly produced thymocytes fail the selection and undergo apoptosis. Apoptotic thymocytes' efficient removal is a prerequisite step



<sup>&</sup>lt;sup>1</sup>Institute of Microbiology and Immunology, National Yang Ming Chiao Tung University, Taipei 112, Taiwan

<sup>&</sup>lt;sup>2</sup>Department of Life Sciences and Institute of Genome Sciences, National Yang Ming Chiao Tung University, Taipei 112, Taiwan

<sup>&</sup>lt;sup>3</sup>Institute of Biomedical Informatics, National Yang Ming Chiao Tung University, Taipei 112, Taiwan

<sup>&</sup>lt;sup>4</sup>Agricultural Biotechnology Research Center, Academia Sinica, Taipei 112, Taiwan

<sup>&</sup>lt;sup>5</sup>Taiwan International Graduate Program in Molecular Medicine, National Yang Ming Chiao Tung University and Academia Sinica, Taipei, Taiwan

<sup>&</sup>lt;sup>6</sup>Lead contact

<sup>\*</sup>Correspondence: clhsu@nycu.edu.tw https://doi.org/10.1016/j.celrep.2022.111065



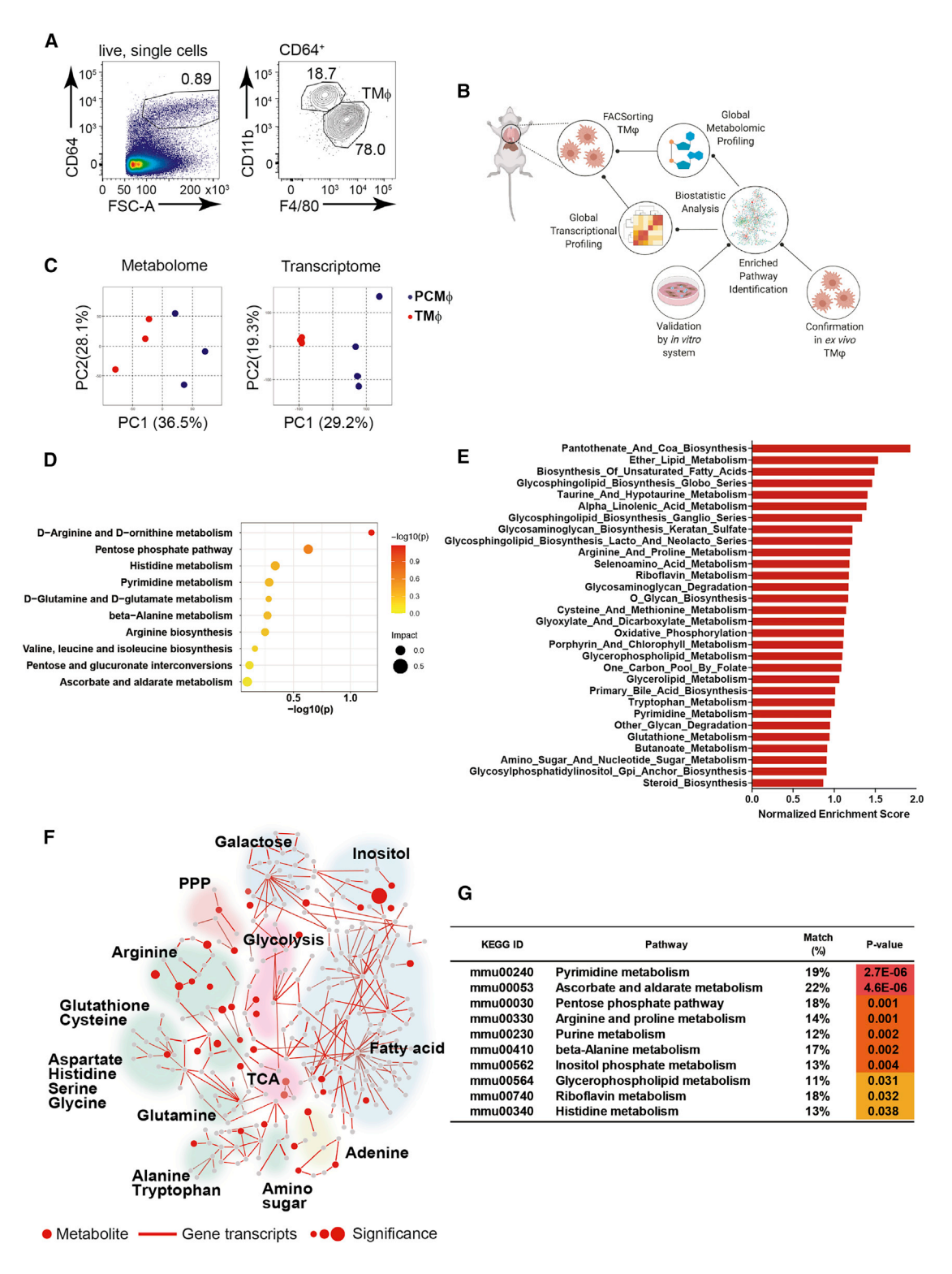


Figure 1. Multiomics analyses revealed that  $TM\phi s$  have a distinct metabolic profile

(A) The thymic single-cell suspension was prepared as described in STAR Methods. Under the live, single-cell gating, the CD64\*F4/80\*CD11b<sup>lo</sup> TMφs or CD11b+F4/80+ PCM $\phi$ s (Figure S1) were sorted (purity > 95%) for further analyses.

- (B) The multiomics and validation design of this study.
- (C) PCA of metabolomics (n = 3) and transcriptomic (n = 3 to 4) results comparing TMφs and PCMφs (Figure S2).
- (D) Identification of the top 10 metabolic pathways that were augmented in TMφs compared with PCMφs using MetaboAnalyst, n = 3.

(legend continued on next page)

### Article



to avoid unwanted auto-inflammation and tissue damage. As the professional phagocytes in the thymus (Surh and Sprent, 1994), resident thymic macrophages (TMφs) only represent 0.1% of total cells in the thymus. We comprehensively examined the phenotype of TMφs and defined them as a CD64+F4/ 80<sup>+</sup>MerTK<sup>+</sup>CD11b<sup>lo</sup> population (Zhou et al., 2021). It is projected that each TM $\phi$  is responsible for the clearance of  $\sim\!50$  apoptotic thymocytes daily, making this cell population a central hub for efferocytosing and processing cell bodies and biomaterials in the thymus. We anticipated that TMφs likely have distinctive metabolic features adapting to the thymic environmental factors and supporting their tissue-specific functional demands.

Efferocytosis is a multistep event to remove apoptotic cells. It involves tightly controlled recognition, signaling events, and metabolic regulation (Boada-Romero et al., 2020; Trzeciak et al., 2021). Disruption of efferocytosis is associated with conditions such as sterile inflammation or autoimmunity (Korns et al., 2011). As the phagocytes engulf apoptotic cells, they have to continuously adjust their metabolic programs throughout the efferocytosis process, and each stage of efferocytosis may rely on a different or combination of metabolic pathways. The initial contact of apoptotic cells upregulates the expression of glucose transporter SLC2A1 and aerobic glycolysis, which fuels the ATP requirements for actin polymerization during phagocytic cup formation (Morioka et al., 2018). The internalization of apoptotic cells then triggers the UCP2 to dissipate the mitochondrial proton gradient (Park et al., 2011), and promotes fatty acid oxidation that further supports the tricarboxylic acid (TCA) cycle and the anti-inflammatory IL-10 production (Zhang et al., 2019). However, in different tissues, the challenges for efferocytosis are much more complicated. Each type of TRM needs to remove the tissue-specific apoptotic cells, which vary in their metabolic compositions. For example, splenic red pulp  $M\phi s$  remove the heme-rich senescent red blood cells, while bone marrow-resident Mos engulf the nucleic acid-packed nucleus expelled from developing erythrocytes. Tumor-associated Mφs phagocytose cancer cells enriched in glycolysis intermediates such as glyceraldehyde 3-phosphate, acetyl-coenzyme A (CoA), and ATP (Ortmayr et al., 2019). The number of apoptotic cells TRMs need to clear also varies greatly. Microglia and astrocytes work together to clear 10,000 dead neurons at homeostatic state per day (Bartheld, 2017; Damisah et al., 2020); TMφs deal with as many as 50 million apoptotic thymocytes daily (Yates, 2014). Moreover, the nutrient and oxygen availability differs between tissues: alveolar Mφs are exposed to 19% of O2, while splenic Mφs exist at 3% of O<sub>2</sub> (Zenewicz, 2017). Even the proximity to blood vessels within the tissue affects the cellular behavior, exemplified by the mammalian target of rapamycin (mTOR)dominated anabolic metabolism in perivascular cancer cells (Kumar et al., 2019). Together, these findings highlight the complexity of efferocytosis, particularly within different tissues.

In this study, we set out to gain in-depth insights into the metabolic signatures in  $TM\phi s$ . We found that  $TM\phi s$  were metabolically distinct from PCMφs. The multiomics analyses revealed that TMφs preferentially used the pentose phosphate pathway (PPP) for glucose catabolism compared with the PCMφs. Dissecting with an in vitro system, we discovered this favorable usage of PPP is in response to the efferocytosis-associated reactive oxygen species (ROS) stress and the resulting reductive-oxidation (redox) demands. Blockade of PPP decreases the efferocytosis competency, which can be rescued via ROS scavengers. These findings reveal that TRMs have diverse metabolic features depending on the residence tissues, and uncover the central role of PPP as a metabolic adaptation for  $TM\phi s$  to support the tissue-specific efferocytosis demand.

#### **RESULTS**

### TM ps have distinct transcriptomic and metabolomic signatures that are dictated by their microenvironment

The thymus is an organ with limited blood supply under physiological conditions due to the proposed blood-thymus barrier (Hale et al., 2002). As the professional phagocytes in the thymus responsible for removing and processing apoptotic thymocytes, we speculated that the  $TM\phi s$  are metabolically active cells adapted to the stress associated with efferocytosis under limited oxygen supply. To understand how TMφs cope with the thymic microenvironment and tissue-specific demands, we applied an integrated omics approach on the CD64<sup>+</sup>F4/80<sup>+</sup>CD11b<sup>lo</sup> TMφs and PCMφs (Figures 1A and S1). Primary TMφs and PCMφs were sorted and subjected to ultra performance liquid chromatography-mass spectrometry (UPLC-MS) and RNA sequencing (RNA-seq) analyses (Figure 1B). Principal component analysis (PCA) showed a marked difference between  $TM\phi s$  and PCMφs in their intracellular metabolite contents (Figure 1C, left). The transcriptomic results further confirmed the distinction between TMφs and PCMφs (Figure 1C, right). These results show the apparent metabolomic differences are accompanied by the transcriptomic changes. The active metabolic pathways in TMφs and PCMφs were identified (Figures 1D and S2) through analyzing the metabolomic results, and distinct metabolic profiles between these Mφ populations were observed. Similar to the finding demonstrating that apoptotic-derived arginine drives efferocytosis (Yurdagul et al., 2020), we found that the arginine and ornithine metabolism is one of the most active metabolic pathways in TMφs. The gene set enrichment analysis (GSEA) with a focus on the Kyoto Encyclopedia of Genes and Genomes database (KEGG)-defined metabolism pathways revealed that the TMφs have more active fatty acid and lipid biosynthesis, and amino acid, pyrimidine, and glutathione metabolism compared with PCMφs (Figure 1E). In contrast, PCMφs are active in arachidonic acid and retinol metabolism (Figure S2).

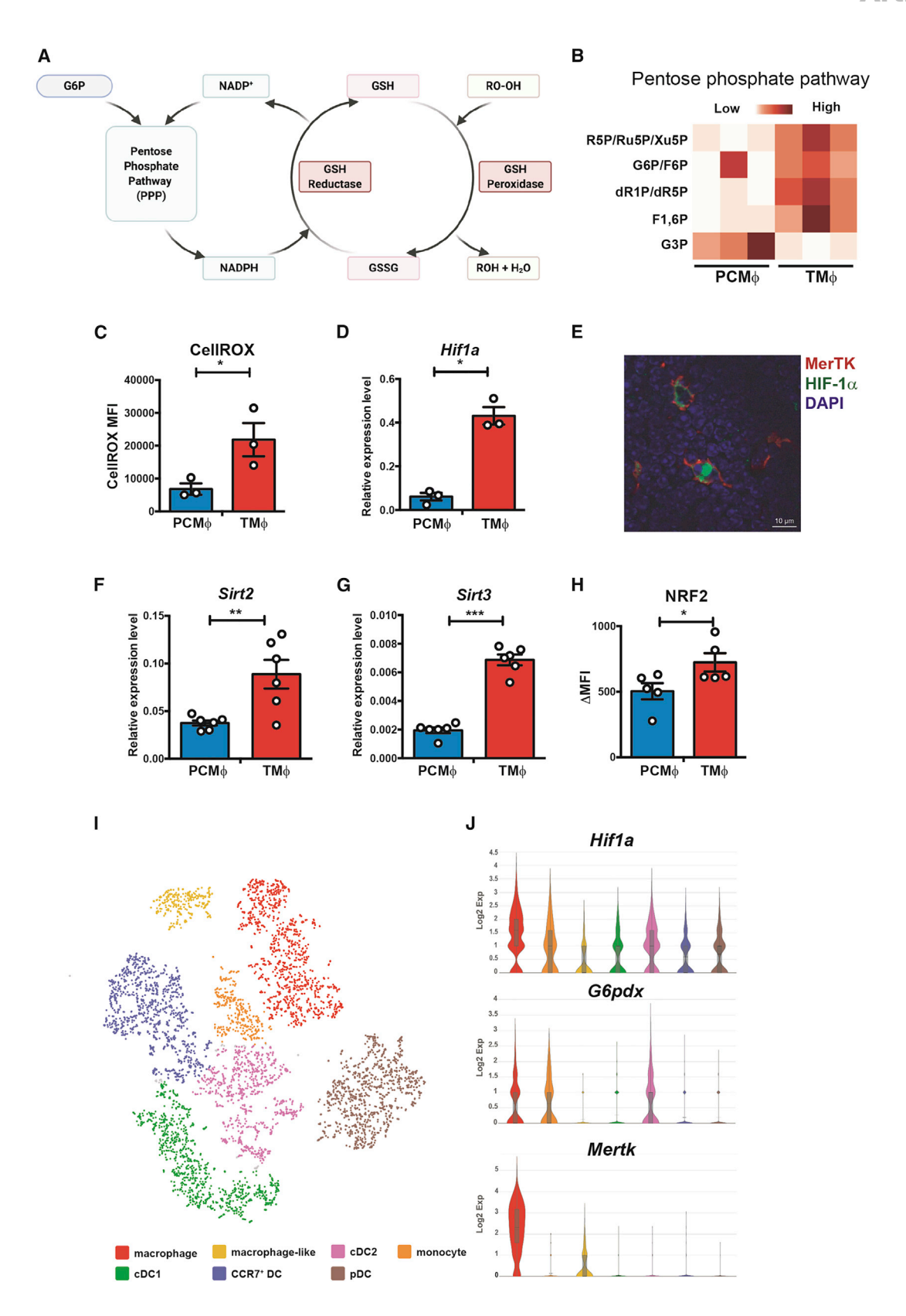
<sup>(</sup>E) GSEA of transcriptomic results showing the top 30 KEGG metabolic pathways that are active in TMφs compared with PCMφs.

<sup>(</sup>F) Joint transcriptomics and metabolomics analysis visualized using GAM (Genes and Metabolites) web-service and Cytoscape open source platform. The upregulated genes are labeled with lines and the metabolites as the circle. Gray represents undetected compounds. The size of the circle or the stick represents the significance of the p value.

<sup>(</sup>G) The enriched KEGG metabolic pathways in TMφs were identified by combining metabolomic and transcriptomic analyses.

The percentage of match was computed by (# of significant upregulated genes and metabolites identified in TMφs)/(# of KEGG defined pathway associated factors), p value was calculated by Fisher's exact test.





### **Article**



We then combined the metabolomic and transcriptomic data into a joint pathway analysis and identified the major metabolic modules in TMφs (Figure 1F), with the corresponding enriched pathways listed in Figure 1G. These results suggest that the Mφs have the plasticity to utilize distinct metabolic pathways that best fit the niche of their resident tissue. Among the extracted results from multiomics analyses, we were particularly intrigued by the higher PPP activity observed in  $TM\phi s$ . As an alternative glucose utilization pathway, PPP is known as a multifaceted metabolic hub. Disturbances in PPP lead to diverse pathologies, including the hemolytic anemia, diabetes, and cancer. However, the contribution of PPP in TRMs has not been explored before. Different from glycolysis, PPP generates NADPH instead of ATP. It is involved in fatty acid metabolism as well as purine/pyrimidine metabolism, which are also identified as highly active metabolic pathways in TMφs, implying a potential central role of PPP in this population.

### The preferential usage of PPP in TM $\phi$ s is closely associated with the oxidative stress and the phagocytosing and degradative demands

In addition to routing glucose into nucleotide and amino acid biosynthesis, PPP is also a major pathway for cellular redox homeostasis (Figure 2A). Having noted the active PPP in  $TM\phi s$ , we wondered if it is a metabolic adaptation to the thymic microenvironment. We compared the abundance of PPP intermediates in  $TM\phi s$  and  $PCM\phi s$  from the UPLC-MS results and found that the PPP-associated metabolites were highly enriched in TMφs (Figure 2B). Intracellular ROS levels were measured, and an increase in ROS was detected in TMφs compared with PCMφs (Figure 2C). These results indicate the ongoing need to reduce the oxidative stress-induced damage in  $TM\phi s$ . In agreement with the observation of cellular ROS, we found that  $TM\phi s$  had a significantly higher level of Hif1a compared with PCMφs (Figure 2D). Immunofluorescent staining of thymic slices also showed strong HIF-1 $\alpha$  signals in TM $\phi$ s (Figures 2E and S3), corroborating that TMφs were under high oxidative stress.

Every cell has a well-orchestrated antioxidant system to balance the level of oxidants and maintain redox homeostasis (Muri and Kopf, 2020). We examined the expression levels of genes known to participate in redox homeostasis: Sirtuin 2, 3 (SIRT2, SIRT3) (Singh et al., 2018) and NF-E2-related factor 2 (Nfe2l2, NRF2) (Tonelli et al., 2018). SIRTs are nicotinamide adenine dinucleotide (NAD)-dependent histone deacetylases (HDACs). SIRT2 deacetylates targets associated with antioxidant- and redox-mediated response, including glucose

6-phosphate dehydrogenase (G6PD), the critical enzyme in PPP that produces NADPH counteracting oxidative stress damage. SIRT3 modulates ROS production via the deacetylation of enzymes responsible for ROS reduction, such as superoxide dismutase 2 (SOD2) and isocitrate dehydrogenase (IDH2). At steady state, NRF2 is a master regulator of antioxidant genes belonging to the leucine zipper family of transcription factors. NRF2 is associated with Kelch-like ECH-associated protein 1 (KEAP1) in the cytosol and undergoes constant proteasomal degradation. Oxidative stress leads to the dissociation of NRF2 from KEAP1 and stabilizes NRF2 for nuclear translocation and binding of antioxidant response elements (AREs). Consistent with ROS's elevation in  $TM\phi s$ , expression profiling showed the significant upregulation of Sirt2 and Sirt3 (Figures 2F and 2G), and the accumulation of NRF2 in TMφs compared with PCMφs (Figure 2H). Consistently, upregulation of NRF2 downstream genes was observed in TMφs (Figure S4A). We reasoned that the elevated ROS in  $TM\phi s$  imposed the need for the redox balance, which calls for the active participation of PPP. These results together suggest that TMφs and PCMφs are metabolically distinct resident Mφs populations, and the high oxidative stress in TMφs is likely the reflection of their distinctive microenvironment.

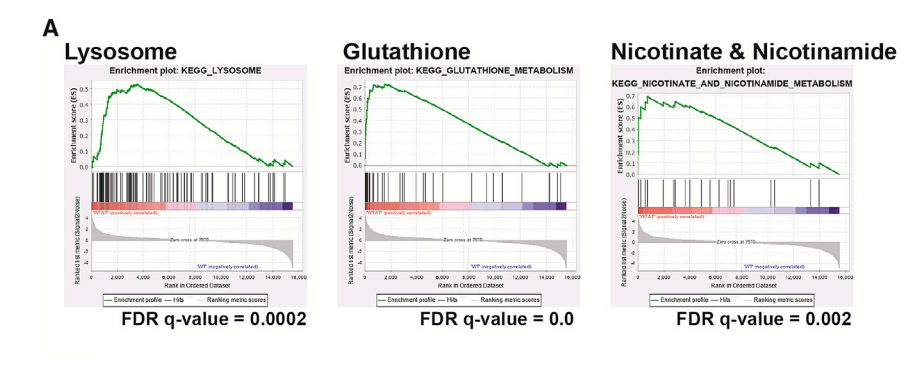
Oxidative stress is intimately linked to oxygen availability. As the thymus is relatively low in oxygen supply, we deliberated if the metabolic adaptation of PPP in TMφs reflects the thymic oxygen tension or is related to the microenvironment-specific functional demands. To delineate these two possibilities, single-cell RNA-seq (scRNA-seq) of the thymic myeloid cell population was performed (Zhou et al., 2021) using the Csf1r-GFP (MaFIA) transgenic mice (Burnett et al., 2004). Seven major myeloid cell subsets were identified in the thymus, including monocyte, TMφ, and dendritic cell (Figure 2I). All myeloid cells expressed various levels of Hif1a echoing the shared low oxygen tension, but TMφs had the highest expression level compared with the other subpopulations. Interestingly, only TMφs, monocyte, and cDC2 had high expression of G6pdx, the rate-limiting enzyme in PPP. We found that the  $TM\phi s$  exclusively have the dominant expression of Mertk, a member of the Tyro-Axl-MerTK (TAM) family of receptor tyrosine kinases (Figure 2J). MerTK is the receptor that mediates the binding and phagocytosis of apoptotic cells (Zagórska et al., 2014). These results confirmed that TMφs are the primary cell population in the thymus responsible for removing apoptotic thymocytes, and the high expression of HIF- $1\alpha$  in TM $\phi$ s is not a general response to the low oxygen availability in the thymic microenvironment. Instead, it is likely

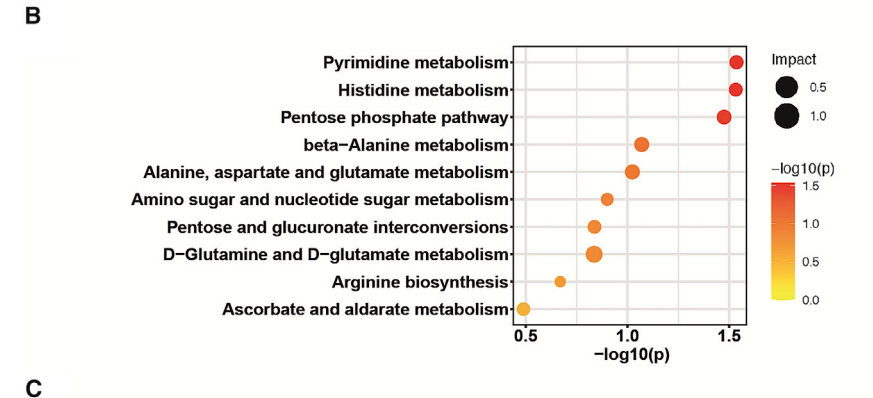
### Figure 2. Oxidative stress responsive factors were upregulated in $TM\phi s$

(A) PPP is the major pathway for cellular redox homeostasis.

- (B) Heatmap showing the abundance of PPP intermediates in TMφs compared with PCMφs detected by UPLC-MS (n = 3).
- (C) The intracellular ROS level of TMφs and PCMφs (n = 3) was evaluated by CellROX staining followed by flow-cytometric analysis.
- (D) The expression of Hif1a in TM $\omega$ s and PCM $\omega$ s was evaluated by gPCR (n = 3).
- (E-H) Thymic slice was immuno-stained with anti-HIF-1α, anti-MerTK, and DAPI for nucleus staining (E) (Figure S3). Scale bar, 10 μm. The mRNA levels of Sirt2 (F), Sirt3 (G), and the protein level of NRF2 (H) in TMφs and PCMφs were measured by qPCR and flow cytometry, respectively (n = 5).
- The expression levels were calculated relative to Rp/19, change in mean fluorescence intensity (\Delta MFI) was calculated by MFI minus fluorescence minus one (FMO) reading. The expression of NRF2-regulated genes in TMφs and PCMφs is shown in Figure S4A.
- (I) scRNA-seq analysis of thymic myeloid cells using MaFIA mice. Distinct myeloid subpopulations were identified, including the TMφ population.
- (J) Violin plots generated from the scRNA-seq results show the expression levels of Hif1a, Mertk, and G6pdx among the identified thymic myeloid subpopulations. Data shown are means  $\pm$  SEM. Unpaired two-tailed Student's t test, \*p < 0.05, \*\*p < 0.01, \*\*\*p < 0.001.







KEGG ID	Pathway	Match (%)	P-value
mmu00480	Glutathione metabolism	24%	3.5E-08
mmu00030	Pentose phosphate pathway	18%	0.003
mmu00340	Histidine metabolism	16%	0.005
mmu00040	Pentose and glucuronate interconversions	15%	0.006
mmu00470	D-Amino acid metabolism	21%	0.008
mmu00982	Metabolism of xenobiotics by cytochrome P450	12%	0.011
mmu00250	Alanine, aspartate and glutamate metabolism	15%	0.021
mmu00053	Ascorbate and aldarate metabolism	14%	0.023
mmu00330	Arginine and proline metabolism	12%	0.027
mmu00220	Arginine biosynthesis	16%	0.032

prompted by their tissue-specific functions, such as the efficient removal of apoptotic thymocytes.

### Efferocytosis is accompanied by oxidative stress

The information obtained from thymic myeloid cell scRNA-seq prompted us to speculate that the removal of apoptotic cells, efferocytosis, is a significant source inducing the oxidative stress in Mφs. We performed transcriptomic and metabolomic analyses on bone marrow-derived macrophages (BMDMs) treated with apoptotic thymocytes to test this possibility. The GSEA showed that the treatment with apoptotic thymocytes was accompanied by an increase in lysosomal activity and resulted in the enrichment of the KEGG pathway for glutathione metabolism and nicotinate and nicotinamide metabolism, implying that active efferocytosis is associated with redox needs (Figure 3A). Furthermore, the upregulation of NRF2 downstream genes in response to the efferocytosis-induced oxidative stress was observed in these Mφs (Figure S4B). The metabolomic and transcriptomic profiling and activity measurements also

Figure 3. Efferocytosis of apoptotic thymocytes is sufficient to augment the oxidative stress and increases the redox demand in

(A) RNA-seq analysis of BMDMs treated with apoptotic thymocytes was subjected to GSEA. The significant enrichment biological processes of the lysosome, glutathione metabolism, and nicotinate/nicotinamide metabolism were identified. (B) Metabolome analysis to identify the enriched metabolic pathways in BMDMs that efferocytosed apoptotic thymocytes, n = 3.

(C) The enriched KEGG metabolic pathways in BMDMs upon apoptotic thymocyte efferocytosis were identified by joint metabolomic and transcriptomic analyses. p value was calculated by Fisher's exact test.

identified PPP as an active metabolic pathway upon efferocytosis in BMDMs (Figures 3B, 3C, and S5). These results collectively suggest that this preferential PPP usage is likely a response to cope with the efferocytosis-associated oxidative stress in Mφs.

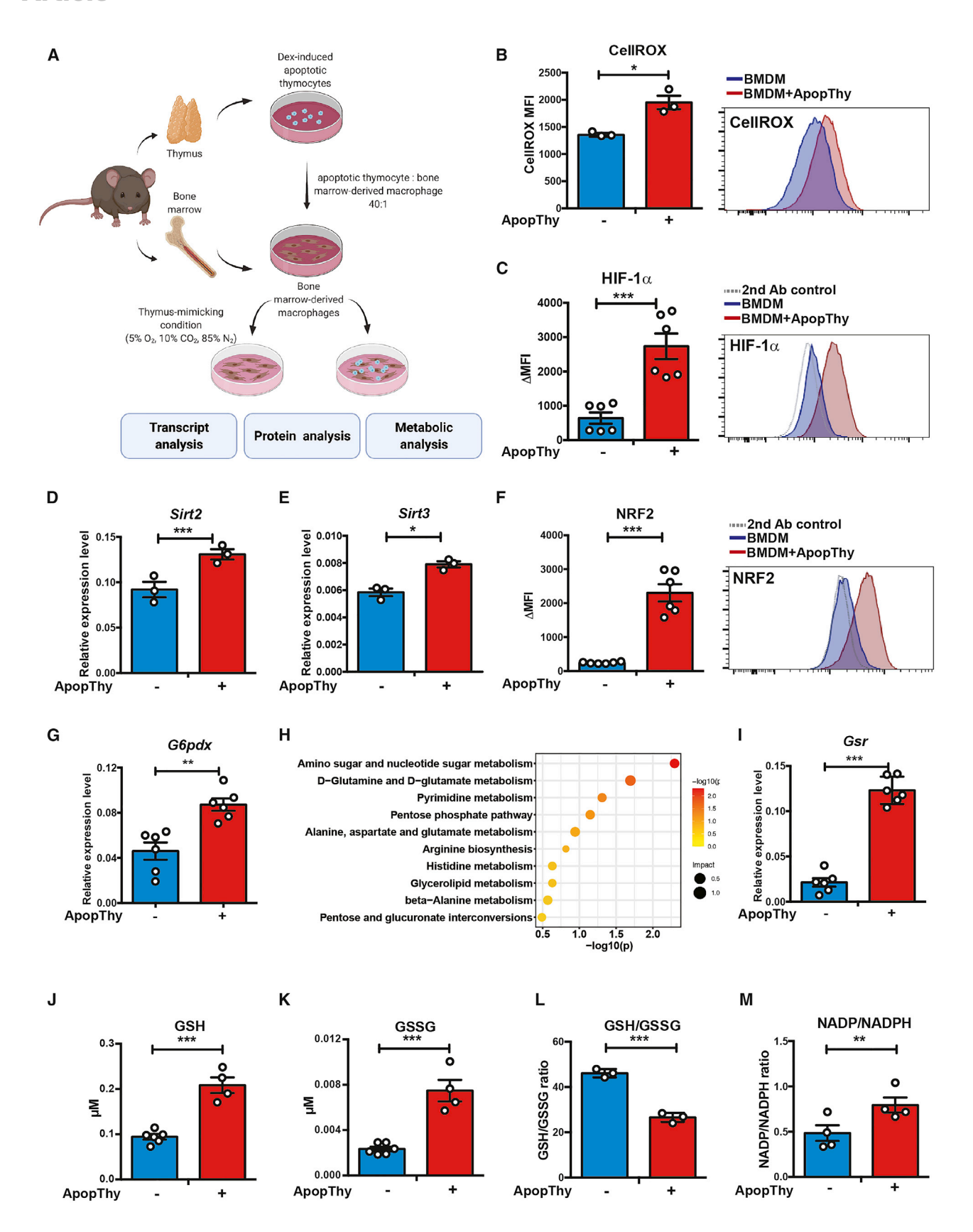
### Efferocytosis of apoptotic thymocytes is the key microenvironmental factor that creates the redox demands in

To scrutinize if the upregulation of PPP in TMφ is an adaptation to its tissue-specific functional demands, we devised an in vitro system imitating the thymic microenvironment (Figure 4A). By treating BMDMs with apoptotic thymocytes in a low-O<sub>2</sub> condition (defined as 5% O<sub>2</sub>, similar to the level found in the thymus

in vivo; Braun et al., 2001; Hale et al., 2002), we observed an elevation of cellular ROS levels (Figure 4B) and the accumulation of HIF-1α (Figure 4C), recapitulating the phenotypes noted with ex vivo TMφs. These results suggested that the efferocytosis of apoptotic thymocytes was accompanied by oxidative stress under this thymic-mimicking condition. The apoptotic thymocyte-engulfing BMDMs augmented the expression of Sirt2 and Sirt3 (Figures 4D and 4E) and had an evident accumulation of NRF2 (Figure 4F) to buffer the excess ROS stress. Under this condition, apparent upregulation of G6pdx was observed (Figure 4G), suggesting the launch of PPP flux. These apoptotic thymocyte-engulfing BMDMs showed a similar metabolic profile as ex vivo TMφs by metabolomic analysis (Figure 4H), further supporting the notion of PPP activation as a metabolic adaptation to process the efferocytosis-associated stress for  $TM\phi s$ . PPP contributes to redox homeostasis via glutathione, the cellular scavenger for hydroxyl radicals, singlet oxygen, and electrophiles. In healthy cells, the majority of the total glutathione pool is in the reduced form (GSH), which is mainly generated via

### Article





(legend on next page)





the conversion of oxidized glutathione (GSSG) by glutathione reductase (encoded by Gsr) with NADPH from the PPP. The upregulation of Gsr was observed in apoptotic thymocyte-engulfing BMDMs (Figure 4I), again verifying the ongoing redox demand in these cells. The ratio of GSH/GSSG present in the cell is a crucial factor for the proper maintenance of the oxidative balance of the cell. While GSH serves as the first line of defense against oxidative stress, GSSG accumulates when cells are exposed to increased levels of oxidative stress. Leukemia cells, for example, reprogram their GSH synthesis to cope with hypoxia-induced oxidative stress (Goto et al., 2014). Both GSH (Figure 4J) and GSSG (Figure 4K) increased significantly while the GSH/GSSG ratio had a marked decrease (Figure 4L) in these apoptotic thymocyte-engulfing BMDMs, indicating the ongoing oxidative stress. Consistent with the engagement of the GSH/ GSSG circuit, the apoptotic thymocyte-treated BMDMs had an augmented NADP/NADPH ratio (Figure 4M) due to the decreased NADPH pool supporting the generation of GSH. Together, these results revealed the active metabolic adaptation to the high redox demands in Mos when performing efferocytosis and explained the favorable PPP usage in  $TM\phi s$ .

### Efferocytosis-associated redox demand drives the preferential glucose flux into PPP

To this point, the results from multiomics analyses on TMφs and the in vitro experiment on efferocytosing BMDMs under low O2 availability converged on the redox demands and suggested the active involvement of PPP. As an alternative glucose catabolism pathway, PPP branches from glucose 6-phosphate (G6P) to produce NADPH and ribose 5-phosphate (R5P) (Figure 5A). We examined if efferocytosis affected the glucose uptake and observed the significantly increased 2-NBDG (2-(N-(7-nitrobenz-2-oxa-1,3-diazol-4-yl)amino)-2-deoxyglucose, a fluorescent glucose analog) accumulation in BMDMs treated with apoptotic thymocytes (Figure 5B). To follow the glucose flow and evaluate its flux into glycolysis and PPP, we performed a <sup>13</sup>C<sub>6</sub>-glucose tracing experiment under both normoxia (20% O<sub>2</sub>) and the thymic microenvironment-mimicking condition (5% O2). We noted that the efferocytosis of apoptotic thymocytes accelerated glucose catabolism compared with the no-treatment group under both conditions (Figure 5C). However, the glucose flux to glycolysis and generation of 3PG was not altered

by efferocytosis (Figure 5D). Instead, an apparent increase of PPP intermediates, including Ru5P/Xu5P, R5P, and S7P, was observed in the presence of active efferocytosis (Figure 5E). Together, these results demonstrated that  $M\phi s$  increase glucose uptake and shunt the glucose to PPP upon the efferocytosis of apoptotic thymocytes. These results suggest that the preferential usage of PPP in  $TM\phi$  is likely a result of handling the efferocytosis demand in the thymic microenvironment.

### Activated PPP supports the efferocytosis capacity of Mφs

Having demonstrated the link between efferocytosis and PPP usage, we pondered the functional importance of the PPP flux in active scavenging Mφs. PPP is the primary source of NADPH, which is used for glutathione reduction, fatty acid synthesis, and pyruvate oxidation to malate. Excessive ROS have been shown to stiffen the  $M\phi s$  membrane and cytoplasm, thus reducing the phagocytic activity (Agarwal et al., 2020). On the other hand, the fatty acid composition on the plasma membrane has been closely linked to the phagocytic capacity (Schumann, 2016), highlighting the importance of fatty acid synthesis in actively phagocytosing  $M\phi s$ . To test if the active PPP supports the efferocytosis-associated events, we applied 6-aminonicotinamide (6-AN), an inhibitor of glucose-6-phosphate dehydrogenase (G6PD) (Preuss et al., 2012), to BMDMs. We found that BMDMs had decreased efferocytosis and its associated ROS when PPP flux was blocked by 6-AN treatment (Figures 6A and 6B). The PPP blockade-induced reduction of efferocytosis was associated with the downregulation of the apoptotic cell sensors MerTK and AXL (Figures 6C and 6D) and altered membrane fluidity (Figure 6E), but not with cytoskeleton dynamics (Figure 6F). Yurdagul et al. (2020) showed that apoptotic cell-derived arginine and ornithine drive the polyamine biosynthesis in  $M\phi s$ . Interestingly, arginine biosynthesis is also a top hit in our metabolomic analysis (Figures 1D and 3B), and we found efferocytosis triggered the polyamine synthesis (Figure 6G). Although blockade of PPP did not significantly alter polyamine synthesis, likely due to 6-AN-mediated inhibition of efferocytosis, N-acetylcysteine (NAC), the thiol-containing antioxidant that scavenges ROS, notably reduced it (Figure 6H). These results imply that PPP and polyamine biosynthesis likely converge at ROS. To further validate the observations with

### Figure 4. In vitro efferocytosis of apoptotic thymocytes under a thymic microenvironment-mimicking condition recapitulates the oxidative stress observed in TMos

(A) Illustration of the experimental setup for the in vitro culture system. BMDMs were treated with dexamethasone-induced apoptotic thymocytes for 24 h under 5% O<sub>2</sub> condition and harvested for analysis.

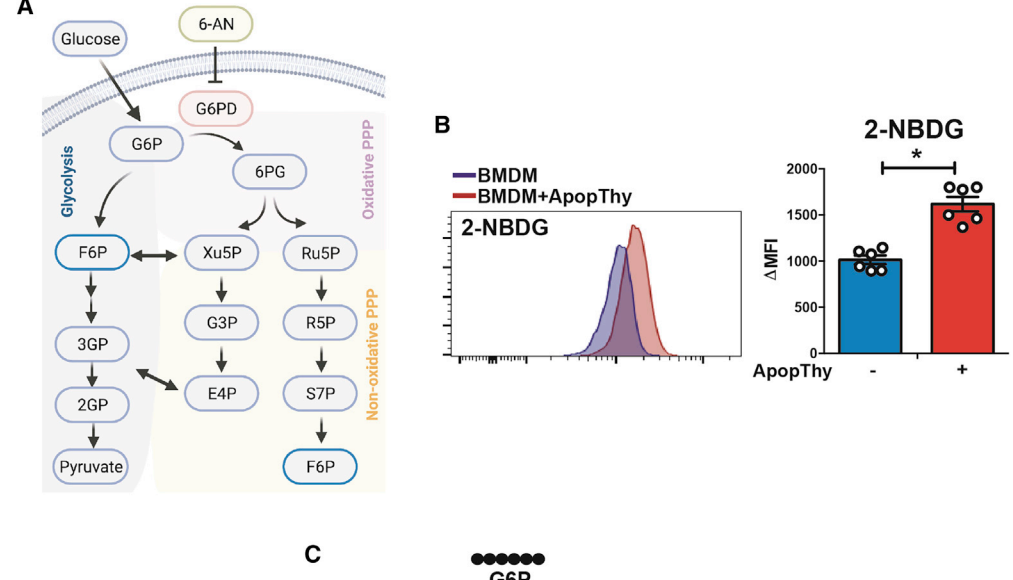
- (B) The intracellular ROS level of apoptotic thymocyte-treated BMDMs was evaluated by CellROX staining and analyzed by flow cytometry (n = 3).
- (C–E) HIF-1α expression was determined by immunostaining followed by flow-cytometric analysis (n = 6) (C). The induction of Sirt2 (D) and Sirt3 (E) by apoptotic thymocyte treatment in BMDMs were evaluated by qPCR (n = 3). The expression levels were calculated relative to Rp/19.
- (F) The amount of NRF2 in BMDMs was quantified by immunostaining followed by flow-cytometric analysis (n = 3). \( \Delta MFI \) was calculated by MFI minus isotype control value. The upregulation of NRF2 downstream genes upon efferocytosis is shown in Figure S4B.
- (G) The expression of G6pdx in BMDMs was determined by qPCR (n = 6).
- (H) The top 10 metabolic pathways augmented in BMDMs upon efferocytosing apoptotic thymocytes were identified by metabolomic analyses (n = 3).
- (I) The induction of Gsr in apoptotic thymocytes-treated BMDMs was measured by qPCR (n = 6).
- (J-L) The concentration of (J) GSH and (K) GSSG in BMDMs upon treatment was measured by luminescent-based assay (n = 3), with the GSH/GSSG ratio shown in (L).

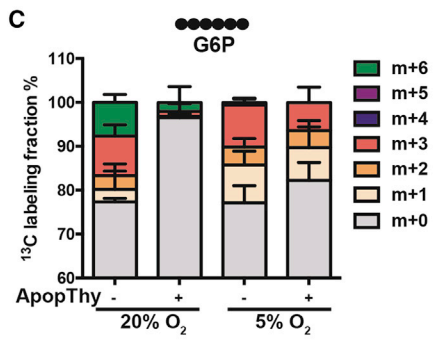
(M) The NADP/NADPH ratio was evaluated with colorimetric assay (n = 4).

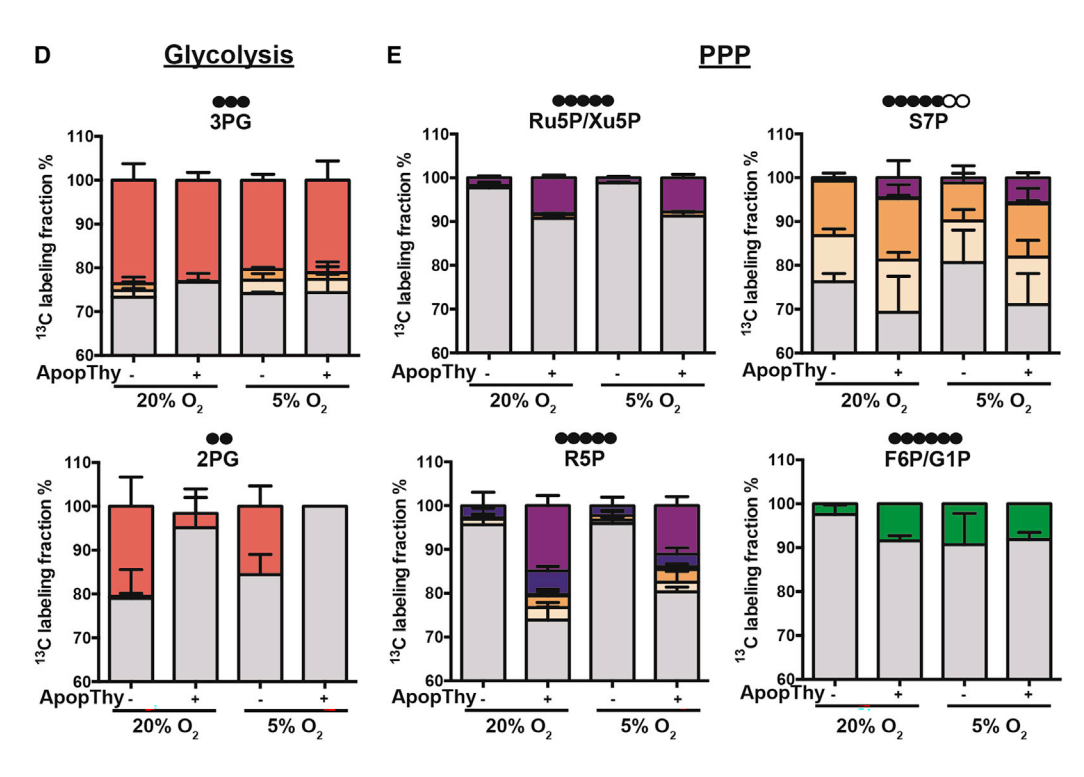
Data shown are means  $\pm$  SEM. One-way ANOVA, \*p < 0.05, \*\*p < 0.01, \*\*\*p < 0.001, n.s., no significance.











(legend on next page)





6-AN treatment, small interfering RNAs (siRNAs) to Nfe2l2 and Gclc were applied to BMDMs. While NRF2 is the key component in response to oxidative stress, GCLC participates in the first and rate-limiting step in glutathione biosynthesis. Consistent with PPP inhibition results, downregulation of NRF2 (Figure 6I) or GCLC (Figure 6J) both significantly affected the efferocytosis of Mφs. These data demonstrate a strong association between redox capacity and phagocytosis efficiency. Together, these results suggest that efferocytosis diverts the glucose flux to PPP to counter the oxidative stress and support the continual engulfment of apoptotic cells in  $M\phi s$ .

### **Dampening the PPP impairs the efficient efferocytosis** and apoptotic thymocyte clearance in the thymus

A thymic explant system was devised to test if the effect of PPP blockade on efferocytosis holds true for TMφs. 6-AN was directly injected into the ROSA26 GFP thymic lobe, incubated, and processed to evaluate the phagocytic capacity in TMφs (Figure 7A). Since all thymocytes are endogenously labeled with GFP in the ROSA26 GFP thymus, the engulfment of apoptotic thymocytes in the TMφs can be evaluated by GFP intensity. Decreased phagocytosis of apoptotic thymocytes was observed in the 6-AN-treated TMφs compared with the solvent control (Figure 7B), validating the importance of PPP flux in supporting TMos efferocytosis ex vivo. The reduced efferocytosis in 6-ANtreated TM<sub>0</sub>s was accompanied by decreased oxidative stress (Figure 7C), solidifying the causal link between efferocytosis and induction of oxidative stress. A similar observation was found in the dexamethasone-induced thymus injury model (Figure S7). To demonstrate the physiological consequence of PPP in TMφs, we performed an intrathymic injection of 6-AN and observed the significant accumulation of apoptotic cells in the thymus in vivo (Figures 7D and 7E). Together, these results revealed that  $TM\phi s$  undergo metabolic adaptation in response to the thymic-specific functional demand of efficiently removing apoptotic thymocytes.

### Knockdown G6PD affects the phagocytic capacity of human Mφs

G6PD is the enzyme in PPP responsible for converting G6P to 6PG and is coupled to the reduction of NADP to NADPH. The G6PD deficiency is the most common inherited enzymopathy, with more than 200 known mutations. It is notable that no known human or murine null mutant has been observed, and some residual enzyme activity is found in all mutant cases (Longo et al., 2002). While G6PD-deficient patients are mostly asymptotic, they can develop acute hemolytic anemia (AHA) when triggered by fava beans or certain drugs (Luzzatto et al., 2020). Some of these G6PD patients experience severe bacterial infections and increased frequency of sepsis, possibly due to the inability to produce enough NADPH during oxidative burst (Corrons et al., 1982). However, G6PD deficiency is also related to autoimmune diseases, including systemic lupus erythematosus (SLE) (Fujii et al., 2015), the autoimmune disease associated with defects in the clearance of apoptotic cells (Elliott and Ravichandran, 2010; Mahajan et al., 2016). We wondered if defective PPP could be one of the pathogenic factors contributing to the autoimmunity association in G6PD deficient patients due to Mφs' reduced capacity to efferocytose. To test this possibility, we used siRNA to knock down G6PD in the human monocytic cell line THP-1-derived M $\varphi$ s (Figure 7F). When co-cultured with apoptotic thymocytes, these G6PD knockdown Mos were less efficient in phagocytosing apoptotic cells (Figure 7G), implying that ineffective apoptotic cell clearance may be a risk factor contributing to autoimmunity development in G6PD patients. To test if loss of redox buffering is the major contributor dampening efferocytosis in G6PD knockdown Mφs, NAC was added to the G6PD knockdown Mφs. NAC treatment significantly rescued the efferocytosis capacity in these G6PD knockdown  $M_{\phi}s$ , although it did not reach control level (Figure 7G). We further validated that the G6PD knockdown-induced defect in efferocytosis could be reversed by the presence of glutathionereduced ethyl ester (GSH-MEE), a membrane-permeable derivative of GSH that supplements the intracellular GSH and reduces reactive species (Figure 7G). Together, these results provided evidence linking PPP and the efferocytosis-induced redox demand in human Mφs and implied a potential therapeutic direction to decrease the autoimmunity risk in G6PD-deficient patients.

### **DISCUSSION**

In summary, the present study uncovers the distinctive metabolic program of the resident  $TM\phi s$ . The comparison between  $TM\phi s$  and  $PCM\phi s$  is an example signifying that different TRMs have distinct metabolic profiles, depending on their microenvironment and functional demands. Our results provide a alimpse into TRM metabolism, and, perhaps more importantly, a demonstration of Mos' flexibility to metabolically adapt to their microenvironment. It is highly possible that each TRM population, which vary extensively in function, has its diversified metabolic program. It is also conceivable that the steady-state metabolism can be rapidly realigned upon pathogen challenge and metabolic disturbance or gradually changed along the aging process. The multiomics analyses in this study show how transcriptional regulation is closely intertwined with cellular metabolism. While advances are being made in gene manipulation, adjustment of cellular metabolism may serve as another powerful tool to modulate the M $\phi$  function. With the apprehension of how M $\phi$ abnormalities have been associated with various diseases

### Figure 5. Efferocytosis drives PPP flux in Mφs

(A) Simplified illustration of glycolysis and PPP.

(B) The glucose uptake in BMDMs was monitored by measuring the 2-NBDG fluorescence by flow-cytometric analysis. ΔMFI was calculated by MFI minus BMDM autofluorescence value (n = 6). To follow the glucose flux, major metabolic intermediates in the glycolytic pathway and PPP were monitored by

(C-E) The BMDMs were treated with apoptotic cells and then pulsed with <sup>13</sup>C<sub>6</sub>-Glucose for 120 min, and subjected to liquid chromatography-mass spectrometry (LC-MS) analysis (n = 3). 13C<sub>6</sub>-labeled G6P (C), glycolysis (D), and PPP intermediates (E) in efferocytosing BMDMs. Data shown are means ± SEM. Unpaired twotailed Student's t test, \*p < 0.05.

### **Cell Reports Article**



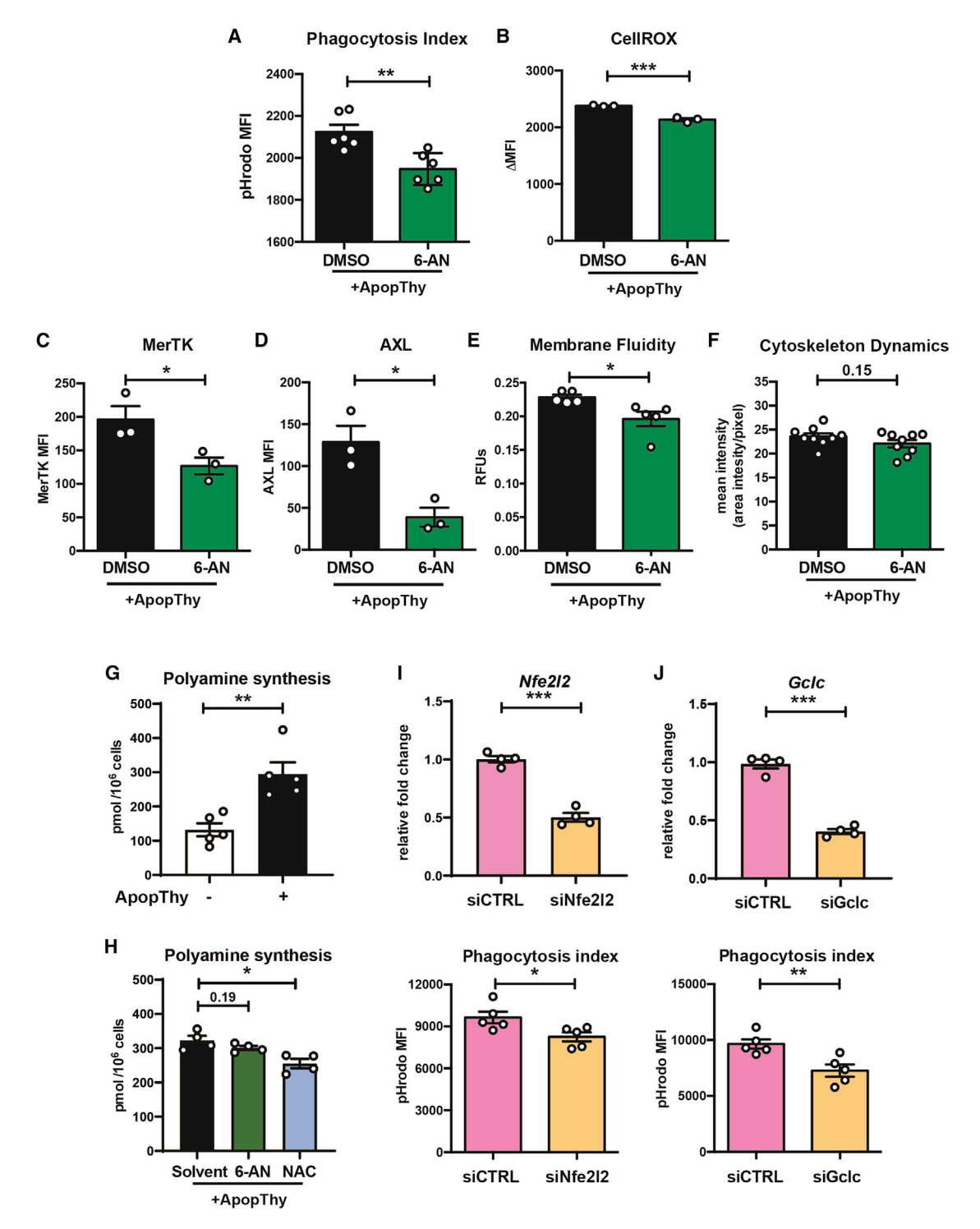


Figure 6. PPP supports the efferocytosis capacity of  $M\phi s$ 

(A) The efferocytosis competency upon 6-AN treatment was examined via detecting the fluorescence emitted from pHrodo-labeled apoptotic cells that had been phagocytosed by BMDMs (n = 6).

- (B) The efferocytosis-associated cellular ROS level upon 6-AN treatment in BMDMs was measured by CellROX staining.
- (C and D) The surface expression of apoptotic cell sensors MerTK (C) or AXL (D) upon PPP blockade (n = 3) was measured by flow-cytometric analysis.
- (E) Evaluation of membrane fluidity upon 6-AN treatment (n = 5).
- (F) The impact of 6-AN on efferocytosing BMDM cytoskeleton dynamics was measured via F-actin staining (n = 9).
- (G and H) The polyamine synthesis in BMDMs (G) upon efferocytosis (n = 5) or (H) in the presence of 6-AN or ROS scavenger (n = 4).
- (I and J) The knockdown efficiency of Nfe2l2 (I) and GcIc (J) and the resulting impacts on BMDM phagocytosis capacity (n = 5).

Data shown are means  $\pm$  SEM. Unpaired two-tailed Student's t test, \*p < 0.05, \*\*p < 0.01, \*\*\*p < 0.001.



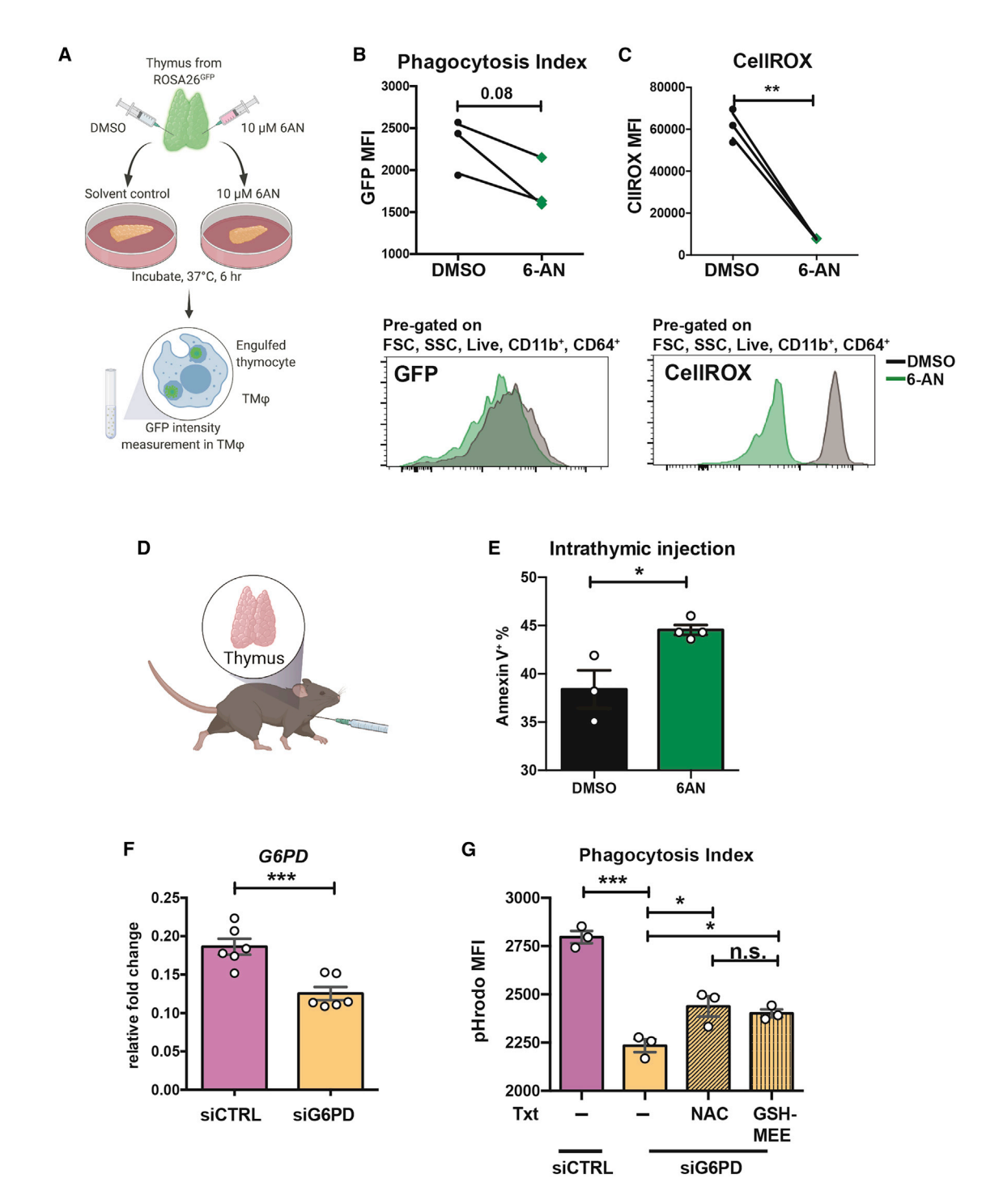


Figure 7. Disturbance of PPP affects efferocytosis and apoptotic cell clearance in the thymus and human  $M\phi$ s

(A) Illustration of the experimental procedures of the PPP blockade in the thymic explant.

(B and C) The efferocytosis capacity of TMφs upon 6-AN treatment was measured by GFP intensity (B), while the cellular ROS level was determined by CellROX staining via flow cytometry (C) (n = 3).

- (D) In vivo alteration of PPP in the thymus via intrathymic injection.
- (E) The accumulation of apoptotic cells upon treatment was measured by Annexin V binding assay and showed in Annexin V<sup>+</sup> percentage (n = 3-4).
- (F) The knockdown efficiency of siRNA to G6PD in THP-1-derived M⊕s was determined by qPCR (n = 3). The expression levels were calculated relative to GAPDH.
- (G) The efferocytosis performance in G6PD knockdown THP-1-derived Mφs and the effects of ROS scavengers, NAC and GSH-MEE, were evaluated by the pHrodo fluorescence intensity generated from phagocytosed apoptotic cells (n = 3).

Data shown are means  $\pm$  SEM. Unpaired two-tailed Student's t test, \*p < 0.05, \*\*p < 0.01, \*\*\*p < 0.001.

### **Article**



(Cox et al., 2021), further understanding of different TRMs with multiomics approaches may be of use for exploring therapeutic opportunities.

The preferential usage of PPP in TMφs and apoptotic thymocyte-phagocytosing BMDMs highlights the versatility of this pathway. The contribution of PPP has been noted for the production of proinflammatory cytokines in M1-M $\phi$  (Muri and Kopf, 2020), the generation of ROS via NADPH oxidase (NOX2), and the antioxidant capacity during the resolution of infection (Koo and Garg, 2019). However, as TRMs are programmed to remove apoptotic cells silently (Roberts et al., 2017), they do not need PPP to fuel the inflammation-associated events under homeostatic conditions. PPP also supplies building blocks for nucleotide and fatty acid synthesis; however, as a differentiated and not highly proliferative population, TMφs have low demand for DNA synthesis. We do not rule out newly made nucleotides being used to modulate cell function via long non-coding RNA or microRNAs (O'Neill et al., 2016) in TMφs; however, targeted analyses are required to test this possibility.

We demonstrated that the association between efferocytosis and PPP is linked to surface expression of apoptotic cell sensors and membrane fluidity, likely the reflection of how PPP contributes to the maintenance of redox balance. Loss of redox homeostasis results in the accumulation of O2-derived free radicals that leads to lipid peroxidation of the polyunsaturated fatty acids in the membrane phospholipids. The peroxidation of membrane lipids disrupts the assembly of cell membranes, which inevitably affects membrane fluidity and lipid-protein interaction dynamics (Catalá, 2014). The application of ROS scavengers is sufficient to partially rescue the efferocytosis under PPP blockade, validating the idea that one of PPP's roles during efferocytosis is to neutralize the ROS. It is also plausible that PPP contributes to the fatty acid synthesis demands during efferocytosis, as enhanced phospholipid synthesis is crucial for the development of Mφs filopodia and cellular organelles such as lysosomes, endoplasmic reticulum (ER), and Golgi network (Ecker et al., 2010). Interestingly, PPP has little to no impact on the dynamic of actin cytoskeleton remolding, suggesting that the transition between monomeric and filamentous actin is supported by other pathways, such as non-canonical glutamine transamination (Merlin et al., 2021). When probing the involvement of non-canonical glutaminolysis in  $TM\phi s$ , we found that the expression glutamine transporter, ASCT2, or the glutaminase-1 (GLS) is not enriched in TMφs (Figure S6), implying the existence of differential metabolic preferences in TRMs.

A recent study by He et al. (2022) showed that PCMφs downregulate PPP upon efferocytosis. They showed that a PPP agonist, AG1, reduces phagocytosis and enhances the inflammatory phenotype of PCMφs. This seemingly contradicting result is an excellent example demonstrating the distinct metabolic adaptation in different TRMs. PCMφs are active in arachidonic acid metabolism (Figure S2), which reflects the peritoneal cavity-specific metabolite milieu (Davies et al., 2017). The metabolite composition in the thymic interstitial fluid has not been explored but will be an interesting future direction to pursue. It is highly plausible that these environmental cues predispose the metabolic characteristics of TRMs and lead to diverse responses to challenges. These results together highlight that the same metabolic pathway can serve various cellular activities depending on the environmental demands.

Consistent with Zhang et al. (2019), we noted the activation of fatty acid metabolism in TMφs, suggesting that the elevation of cellular ROS may be the product of increased fatty acid oxidation in TMφs and efferocytosing BMDMs. The thymus is an immunetolerant microenvironment that has abundant expression of the type 2 cytokine IL-4 (Miller et al., 2018). It is also plausible that, to maintain the alternatively activated state of  $TM\phi s$ , the SREBP-1-mediated de novo lipogenesis consumes NADPH (Bidault et al., 2021), which contributes to the rise of ROS levels. Another possible scenario for ROS elevation upon efferocytosis is the need for LC3-associated phagocytosis (LAP) to process the engulfed dying cells (Boada-Romero et al., 2020). We did observe the colocalization of LC3 and TUNEL+ apoptotic cells in the TMφs (Figure S8), suggesting that LAP is active in this cell population. However, further investigation is needed to address the involvement of LAP for TMφs efferocytosis.

The functional demand to constantly remove failed-selection thymocytes poses an enormous metabolic burden on TMos. The engulfment of the apoptotic cell is an energy-consuming event as ATP is required for the actin dynamics and cytoskeletal rearrangements. It has been shown in vitro that  $M\phi s$  increase glucose uptake (Morioka et al., 2018) and convert glutamine through noncanonical transaminase pathways (Merlin et al., 2021) to fuel the efferocytosis. However, TRMs face additional challenges such as the nutrient and O<sub>2</sub> availability or the composition of interacting cells, which vary greatly among tissues. Taking tumor-associated  $M\phi s$ , for example, cancer cells and immune effector cells compete for limited glucose availability. This competition drives TAMs preferentially employing oxidative phosphorylation and expressing the immunosuppressive programmed death-ligand 1 (PD-L1) (Vitale et al., 2019). It is unclear if the specific "metabolite secretome" released from the tissue microenvironment or the act of processing the cellular contents of apoptotic cells regulates the metabolic program of TRMs. Moreover, different modes of cell death induction release different pools of metabolite (Medina et al., 2020). The disparities or similarities among different TRMs' metabolic features remain to be investigated. Future in-depth analyses focusing on different metabolite-sensing modules (Wang and Lei, 2018) in TRMs may shed light on how the microenvironmental secretomes shape cellular metabolism.

Once the apoptotic cell is engulfed, the  $M\phi s$  need to process large quantities of biomaterials, including membrane, nucleic acids, and cell-type-specific abundant substances. These cellular components are degraded, utilized, or exported out of  $M\phi s$  for redistribution to neighboring cells. The apoptotic cell-derived arginine and ornithine, for example, can promote the production of putrescine and activate the Rac-1-mediated efferocytosis (Yurdagul et al., 2020). We found that the key enzymes in polyamine synthesis, Odc1 and Sat1, are both highly expressed in TMφs, suggesting a similar regulatory mechanism may exist in TRMs, including Mφs in atherosclerotic lesions and TMφs. Among TRMs,  $TM\phi s$  are particularly active in decomposing the cell debris and expelling the biomaterials needed for the fast proliferating thymocytes, a demand that requires metabolite transporters expression program. It is tempting to speculate that TRMs share the core metabolite transporter program yet have specialized features





depending on their local microenvironment. Moreover, it is an exciting topic for future studies to investigate the role of  $TM\phi s$ as a central recycling hub to return metabolites derived from apoptotic thymocytes to the thymic microenvironment and support the proliferation of immature thymocytes.

TMφs are constantly under high ROS stress, which can be detrimental to cell survival. Gerlach et al. (2021) recently reported that the apoptotic-derived nucleotides can drive the proliferation of efferocytes. Surprisingly, in our related study (Zhou et al., 2021), we found that TMφs are low proliferating, self-renewing cells at homeostatic state. However, when the acute injury was introduced to the thymus, such as dexamethasone treatment, a clear influx of monocytes was observed. Further studies are needed to understand how this population is maintained and the contribution of their metabolic adaptation. What is the impact of aging on TMφs? Does the spatial location regulate TMφs' metabolic program? Tools facilitating  $TM\phi$ -specific gene manipulation and methods for efficient compound delivery to the thymic microenvironment are needed to understand the impact of TMφs' metabolic features on thymopolesis or relevance to autoimmunity or immunodeficiency in vivo.

#### **Limitations of the study**

Potential limitations associated with the multiomic analyses on sorted ex vivo TMφs are the processing- and sorting-related stress, and the omission of less stable metabolites. The effects of re-oxygenation during sample preparation cannot be excluded. To address the long-term in vivo functional involvement of PPP in TMφs, proper tools such as TMφs-specific Cre animal models are needed.

### **STAR**\*METHODS

Detailed methods are provided in the online version of this paper and include the following:

- KEY RESOURCES TABLE
- RESOURCE AVAILABILITY
  - Lead contact
  - Materials availability
  - Data and code availability
- EXPERIMENTAL MODEL AND SUBJECT DETAILS
- METHOD DETAILS
  - O Bone marrow-derived macrophages
  - THP-1 derived macrophage
  - Tissue-resident macrophage preparation
  - Immunofluorescence staining
  - Reactive oxygen species measurement
  - RNA extraction and Quantitative RT-PCR
  - O Intracellular staining for flow cytometric analysis
  - Metabolomics of tissue-resident macrophages
  - Metabolomics pathway enrichment
  - Gene set enrichment analysis
  - Combined pathway enrichment analysis
  - Single-cell RNA sequencing
  - O Apoptotic thymocytes preparation and treatment to **BMDMs**
  - RNA sequencing of BMDMs

- GSH/GSSG detection
- NADP/NADPH detection
- 2-NBDG uptake assay
- <sup>13</sup>C<sub>6</sub>-glucose tracing
- O Inhibition of pentose phosphate pathway by 6-AN or siRNA
- Phagocytosis assay
- Reactive oxygen species scavengers
- Treatment of thymus explants
- Membrane fluidity measurement
- Cytoskeleton dynamics
- Total polyamine measurement
- O Dexamethasone-induced injury model
- Intrathymic injection
- Apoptotic cell labeling in thymus
- QUANTIFICATION AND STATISTICAL ANALYSIS

#### SUPPLEMENTAL INFORMATION

Supplemental information can be found online at https://doi.org/10.1016/j. celrep.2022.111065.

### **ACKNOWLEDGMENTS**

We would like to thank Dr. Ching-Hua Kuo (NTU) and Shan-An Chan (Agilent Technology) for the support in setting up the <sup>13</sup>C<sub>6</sub>-glucose tracing system. Shuan-Ting Chu helped with the bioinformatics analysis, and we thank Dr. Cheng-Yen Kao for sharing the hypoxia chamber with us. The RNA-seq and scRNA-seq were supported and performed at the Genomics Center for Clinical and Biotechnological Applications of NCFB by Wan-Chun Chang, Bingxiu Guo, Chien-Yi Tung, and Kate Hua. This work was funded by MOST 108-2628-B-010-005, 109-2628-B-010-016, and CPRC NYCU, from the Higher Education Sprout Project by MOE to C.-L.H.

### **AUTHOR CONTRIBUTIONS**

T.-L.T., T.-A.Z., Y.-T.H., J.-C.W., C.-H.H., H.-K.C., H.-H.F., P.-Y.T., Y.-C.H., and H.-K.F. performed the experiments. C.-C.L. and C.-H.L. supported the metabolomics and bioinformatics analyses. C.-Y.L. set up the <sup>13</sup>C<sub>6</sub>-glucose tracing platform. I.L.D. and C.-L.H. conceptualized the study and designed and supervised the experiments. T.-L.T. and C.-L.H. analyzed and interpreted the data and wrote the manuscript.

### **DECLARATION OF INTERESTS**

The authors declare no competing interests.

Received: December 23, 2021 Revised: May 7, 2022 Accepted: June 16, 2022 Published: July 12, 2022

### **REFERENCES**

Agarwal, M., Biswas, P., Bhattacharya, A., and Sinha, D.K. (2020). Reactive oxygen species-mediated cytoplasmic stiffening impairs the phagocytic ability of the macrophage. J. Cell Sci. 133, jcs236471-12. https://doi.org/10.1242/ ics.236471.

Aguilar, S.V., Aguilar, O., Allan, R., Ad David Amir, E., Angeli, V., Artyomov, M.N., Asinovski, N., Astarita, J., Austen, K.F., Bajpai, G., et al. (2020). ImmGen at 15. Nat. Immunol., 1-4. https://doi.org/10.1038/s41590-020-0687-4.

von Bartheld, C.S. (2017). Myths and truths about the cellular composition of the human brain: a review of influential concepts. J. Chem. Neuroanat. 93, 2-15. https://doi.org/10.1016/j.jchemneu.2017.08.004.

### **Article**



Bidault, G., Virtue, S., Petkevicius, K., Jolin, H.E., Dugourd, A., Guénantin, A.C., Leggat, J., Mahler-Araujo, B., Lam, B.Y.H., Ma, M.K., et al. (2021). SREBP1-induced fatty acid synthesis depletes macrophages antioxidant defences to promote their alternative activation. Nat. Metab. 3, 1150-1162. https://doi.org/10.1038/s42255-021-00440-5.

Blériot, C., Chakarov, S., and Ginhoux, F. (2020). Determinants of resident tissue macrophage identity and function. Immunity 52, 957-970. https://doi.org/ 10.1016/i.immuni.2020.05.014.

Boada-Romero, E., Martinez, J., Heckmann, B.L., and Green, D.R. (2020). The clearance of dead cells by efferocytosis. Nat. Rev. Mol. Cell Biol. 21, 398-414. https://doi.org/10.1038/s41580-020-0232-1.

Bohlen, C.J., Bennett, F.C., Tucker, A.F., Collins, H.Y., Mulinyawe, S.B., and Barres, B.A. (2017). Diverse requirements for microglial survival, specification, and function revealed by defined-medium cultures. Neuron 94, 759-773.e8. https://doi.org/10.1016/j.neuron.2017.04.043.

Braun, R.D., Lanzen, J.L., Snyder, S.A., and Dewhirst, M.W. (2001). Comparison of tumor and normal tissue oxygen tension measurements using OxyLite or microelectrodes in rodents. Am. J. Physiol. Heart Circ. Physiol. 280, H2533-H2544. https://doi.org/10.1152/ajpheart.2001.280.6.H2533.

Burnett, S.H., Kershen, E.J., Zhang, J., Zeng, L., Straley, S.C., Kaplan, A.M., and Cohen, D.A. (2004). Conditional macrophage ablation in transgenic mice expressing a Fas-based suicide gene. J. Leukoc. Biol. 75, 612-623. https:// doi.org/10.1189/ilb.0903442.

Catalá, Á. (2014). Lipid peroxidation modifies the assembly of biological membranes "The Lipid Whisker Model". Front. Physiol. 5, 520. https://doi.org/10. 3389/fphys.2014.00520.

Chong, J., Wishart, D.S., and Xia, J. (2019). Using MetaboAnalyst 4.0 for comprehensive and integrative metabolomics data analysis. Curr. Protoc. Bioinf. 68, e86. https://doi.org/10.1002/cpbi.86.

Vives Corrons, J.L., Feliu, E., Pujades, M.A., Cardellach, F., Rozman, C., Carreras, A., Jou, J.M., Vallespí, M.T., and Zuazu, F.J. (1982). Severe glucose-6-phosphate dehydrogenase (G6PD) deficiency associated with chronic hemolytic anemia, granulocyte dysfunction, and increased Susceptibility to infections: description of a new molecular variant (G6PD barcelona). Blood 59, 428-434. https://doi.org/10.1182/blood.V59.2.428.428.

Cox, N., Pokrovskii, M., Vicario, R., and Geissmann, F. (2021). Origins, biology, and diseases of tissue macrophages. Annu. Rev. Immunol. 39, 313-344. https://doi.org/10.1146/annurev-immunol-093019-111748.

Damisah, E.C., Hill, R.A., Rai, A., Chen, F., Rothlin, C.V., Ghosh, S., and Grutzendler, J. (2020). Astrocytes and microglia play orchestrated roles and respect phagocytic territories during neuronal corpse removal in vivo. Sci. Adv. 6, eaba3239. https://doi.org/10.1126/sciadv.aba3239.

Davies, L.C., Rice, C.M., Palmieri, E.M., Taylor, P.R., Kuhns, D.B., and McVicar, D.W. (2017). Peritoneal tissue-resident macrophages are metabolically poised to engage microbes using tissue-niche fuels. Nat. Commun. 8, 2074. https://doi.org/10.1038/s41467-017-02092-0.

Ecker, J., Liebisch, G., Englmaier, M., Grandl, M., Robenek, H., and Schmitz, G. (2010). Induction of fatty acid synthesis is a key requirement for phagocytic differentiation of human monocytes. Proc. Natl. Acad. Sci. USA 107, 7817-7822. https://doi.org/10.1073/pnas.0912059107.

Elliott, M.R., and Ravichandran, K.S. (2010). Clearance of apoptotic cells: implications in health and disease. J. Cell Biol. 189, 1059-1070. https://doi.org/ 10.1083/jcb.201004096.

Fan, H.-H., Tsai, T.-L., Dzhagalov, I.L., and Hsu, C.-L. (2021). Evaluation of mitochondria content and function in live cells by multicolor flow cytometric analysis. Methods Mol. Biol. 2276, 203-213. https://doi.org/10.1007/978-1-0716-1266-8 15.

Fujii, J., Kurahashi, T., Konno, T., Homma, T., and Iuchi, Y. (2015). Oxidative stress as a potential causal factor for autoimmune hemolytic anemia and systemic lupus erythematosus. World J. Nephrol. 4, 213-222. https://doi.org/10. 5527/wjn.v4.i2.213.

Gautier, E.L., Ivanov, S., Williams, J.W., Huang, S.C.-C., Marcelin, G., Fairfax, K., Wang, P.L., Francis, J.S., Leone, P., Wilson, D.B., et al. (2014). Gata6 regulates aspartoacylase expression in resident peritoneal macrophages and controls their survival. J. Exp. Med. 211, 1525-1531. https://doi.org/10. 1084/iem.20140570.

Gerlach, B.D., Ampomah, P.B., Yurdagul, A., Jr., Liu, C., Lauring, M.C., Wang, X., Kasikara, C., Kong, N., Shi, J., Tao, W., and Tabas, I. (2021). Efferocytosis induces macrophage proliferation to help resolve tissue injury. Cell Metab. 33, 2445-2463.e8. https://doi.org/10.1016/j.cmet.2021.10.015.

Gosselin, D., Link, V.M., Romanoski, C.E., Fonseca, G.J., Eichenfield, D.Z., Spann, N.J., Stender, J.D., Chun, H.B., Garner, H., Geissmann, F., and Glass, C.K. (2014). Environment drives selection and function of enhancers controlling tissue-specific macrophage identities. Cell 159, 1327-1340. https://doi. org/10.1016/j.cell.2014.11.023.

Goto, M., Miwa, H., Suganuma, K., Tsunekawa-Imai, N., Shikami, M., Mizutani, M., Mizuno, S., Hanamura, I., and Nitta, M. (2014). Adaptation of leukemia cells to hypoxic condition through switching the energy metabolism or avoiding the oxidative stress. BMC Cancer 14, 76. https://doi.org/10.1186/1471-2407-14-76.

Guilliams, M., and Svedberg, F.R. (2021). Does tissue imprinting restrict macrophage plasticity? Nat. Immunol. 22, 118-127. https://doi.org/10.1038/ s41590-020-00849-2.

Guilliams, M., Thierry, G.R., Bonnardel, J., and Bajénoff, M. (2020). Establishment and maintenance of the macrophage niche. Immunity 52, 434-451. https://doi.org/10.1016/j.immuni.2020.02.015.

Haldar, M., Kohyama, M., So, A.Y.-L., KC, W., Wu, X., Briseño, C.G., Satpathy, A.T., Kretzer, N.M., Arase, H., Rajasekaran, N.S., et al. (2014). Heme-mediated SPI-C induction promotes monocyte differentiation into iron-recycling macrophages. Cell 156, 1223-1234. https://doi.org/10.1016/j.cell.2014.01.069.

Hale, L.P., Braun, R.D., Gwinn, W.M., Greer, P.K., and Dewhirst, M.W. (2002). Hypoxia in the thymus: role of oxygen tension in thymocyte survival. Am. J. Physiol. Heart Circ. Physiol. 282, H1467-H1477. https://doi.org/10.1152/ajpheart.00682.2001.

He, D., Mao, Q., Jia, J., Wang, Z., Liu, Y., Liu, T., Luo, B., and Zhang, Z. (2022). Pentose phosphate pathway regulates tolerogenic apoptotic cell clearance and immune tolerance. Front. Immunol. 12, 797091. https://doi.org/10.3389/ fimmu 2021 797091/full

Heng, T.S.P., and Painter, M.W.; Immunological Genome Project Consortium (2008). The Immunological Genome Project: networks of gene expression in immune cells. Nat. Immunol. 9, 1091-1094. https://doi.org/10.1038/ni1008-1091.

Jang, C., Hui, S., Zeng, X., Cowan, A.J., Wang, L., Chen, L., Morscher, R.J., Reyes, J., Frezza, C., Hwang, H.Y., et al. (2019). Metabolite exchange between mammalian organs quantified in Pigs. Cell Metab. 30, 594–606.e3. https://doi. org/10.1016/j.cmet.2019.06.002.

Jin, N., Bi, A., Lan, X., Xu, J., Wang, X., Liu, Y., Wang, T., Tang, S., Zeng, H., Chen, Z., et al. (2019). Identification of metabolic vulnerabilities of receptor tyrosine kinases-driven cancer. Nat. Commun. 10, 2701. https://doi.org/10. 1038/s41467-019-10427-2.

Koo, S.-J., and Garg, N.J. (2019). Metabolic programming of macrophage functions and pathogens control. Redox Biol. 24, 101198. https://doi.org/10. 1016/j.redox.2019.101198.

Korns, D., Frasch, S.C., Fernandez-Boyanapalli, R., Henson, P.M., and Bratton, D.L. (2011). Modulation of macrophage efferocytosis in inflammation. Front. Immunol. 2, 57. https://doi.org/10.3389/fimmu.2011.00057.

Kumar, S., Sharife, H., Kreisel, T., Mogilevsky, M., Bar-Lev, L., Grunewald, M., Aizenshtein, E., Karni, R., Paldor, I., Shlomi, T., and Keshet, E. (2019). Intra-tumoral metabolic zonation and resultant phenotypic diversification are dictated by blood vessel proximity. Cell Metab. 30, 201-211.e6. https://doi.org/10. 1016/i.cmet.2019.04.003.

Longo, L., Vanegas, O.C., Patel, M., Rosti, V., Li, H., Waka, J., Merghoub, T., Pandolfi, P.P., Notaro, R., Manova, K., and Luzzatto, L. (2002). Maternally transmitted severe glucose 6-phosphate dehydrogenase deficiency is an embryonic lethal. EMBO J. 21, 4229-4239. https://doi.org/10.1093/emboj/ cdf426.





Luzzatto, L., Ally, M., and Notaro, R. (2020). Glucose-6-phosphate dehydrogenase deficiency. Blood 136, 1225-1240. https://doi.org/10.1182/blood.

Mahajan, A., Herrmann, M., and Muñoz, L.E. (2016). Clearance deficiency and cell death pathways: a model for the Pathogenesis of SLE, Front, Immunol, 7, 35. https://doi.org/10.3389/fimmu.2016.00035.

Medina, C.B., Mehrotra, P., Arandjelovic, S., Perry, J.S.A., Guo, Y., Morioka, S., Barron, B., Walk, S.F., Ghesquière, B., Krupnick, A.S., et al. (2020). Metabolites released from apoptotic cells act as tissue messengers. Nature 580, 130-135. https://doi.org/10.1038/s41586-020-2121-3.

Merlin, J., Ivanov, S., Dumont, A., Sergushichev, A., Gall, J., Stunault, M., Ayrault, M., Vaillant, N., Castiglione, A., Swain, A., et al. (2021). Non-canonical glutamine transamination sustains efferocytosis by coupling redox buffering to oxidative phosphorylation. Nat. Metab. 3, 1313-1326. https://doi.org/10. 1038/s42255-021-00471-v.

Miller, C.N., Proekt, I., von Moltke, J., Wells, K.L., Rajpurkar, A.R., Wang, H., Rattay, K., Khan, I.S., Metzger, T.C., Pollack, J.L., et al. (2018). Thymic tuft cells promote an IL-4-enriched medulla and shape thymocyte development. Nature 559, 627-631. https://doi.org/10.1038/s41586-018-0345-2.

Mootha, V.K., Lindgren, C.M., Eriksson, K.-F., Subramanian, A., Sihag, S., Lehar, J., Puigserver, P., Carlsson, E., Ridderstråle, M., Laurila, E., et al. (2003). PGC-1alpha-responsive genes involved in oxidative phosphorylation are coordinately downregulated in human diabetes. Nat. Genet. 34, 267–273. https:// doi.org/10.1038/ng1180.

Morioka, S., Perry, J.S.A., Raymond, M.H., Medina, C.B., Zhu, Y., Zhao, L., Serbulea, V., Onengut-Gumuscu, S., Leitinger, N., Kucenas, S., et al. (2018). Efferocytosis induces a novel SLC program to promote glucose uptake and lactate release. Nature 563, 714-718. https://doi.org/10.1038/s41586-018-0735-5.

Muri, J., and Kopf, M. (2020). Redox regulation of immunometabolism. Nat. Rev. Immunol. 21, 363-381. https://doi.org/10.1038/s41577-020-00478-8.

O'Neill, L.A.J., Kishton, R.J., and Rathmell, J. (2016). A guide to immunometabolism for immunologists. Nat. Rev. Immunol. 16, 553-565. https://doi.org/

Okabe, Y., and Medzhitov, R. (2014). Tissue-specific signals control reversible program of localization and functional Polarization of macrophages. Cell 157, 832-844. https://doi.org/10.1016/j.cell.2014.04.016.

Ortmayr, K., Dubuis, S., and Zampieri, M. (2019). Metabolic profiling of cancer cells reveals genome- wide crosstalk between transcriptional regulators and metabolism. Nat. Commun. 10, 1841. https://doi.org/10.1038/s41467-019-09695-9

Park, D., Han, C.Z., Elliott, M.R., Kinchen, J.M., Trampont, P.C., Das, S., Collins, S., Lysiak, J.J., Hoehn, K.L., and Ravichandran, K.S. (2011). Continued clearance of apoptotic cells critically depends on the phagocyte Ucp2 protein. Nature 477, 220-224. https://doi.org/10.1038/nature10340.

Preuss, J., Richardson, A.D., Pinkerton, A., Hedrick, M., Sergienko, E., Rahlfs, S., Becker, K., and Bode, L. (2012). Identification and characterization of novel human glucose-6-phosphate dehydrogenase inhibitors. J. Biomol. Screen 18, 286-297. https://doi.org/10.1177/1087057112462131.

Ribatti, D. (2015). The discovery of the blood-thymus barrier. Immunol. Lett. 168, 325-328. https://doi.org/10.1016/j.imlet.2015.10.014.

Roberts, A.W., Lee, B.L., Deguine, J., John, S., Shlomchik, M.J., and Barton, G.M. (2017). Tissue-resident macrophages are locally programmed for silent clearance of apoptotic cells. Immunity 47, 913-927.e6. https://doi.org/10. 1016/j.immuni.2017.10.006.

Schumann, J. (2016). It is all about fluidity: fatty acids and macrophage phagocytosis. Eur. J. Pharmacol. 785, 18-23. https://doi.org/10.1016/j.ejphar.2015.

Sergushichev, A.A., Loboda, A.A., Jha, A.K., Vincent, E.E., Driggers, E.M., Jones, R.G., Pearce, E.J., and Artyomov, M.N. (2016). GAM: a web-service for integrated transcriptional and metabolic network analysis. Nucleic Acids Res. 44, W194-W200. https://doi.org/10.1093/nar/gkw266.

Shannon, P., Markiel, A., Ozier, O., Baliga, N.S., Wang, J.T., Ramage, D., Amin, N., Schwikowski, B., and Ideker, T. (2003). Cytoscape: a software environment for integrated models of biomolecular interaction networks. Genome Res. 13. 2498-2504. https://doi.org/10.1101/gr.1239303.

Singh, C.K., Chhabra, G., Ndiaye, M.A., Garcia-Peterson, L.M., Mack, N.J., and Ahmad, N. (2018). The role of Sirtuins in antioxidant and redox signaling. Antioxid. Redox Signal. 28, 643-661. https://doi.org/10.1089/ ars.2017.7290.

Subramanian, A., Tamayo, P., Mootha, V.K., Mukherjee, S., Ebert, B.L., Gillette, M.A., Paulovich, A., Pomeroy, S.L., Golub, T.R., Lander, E.S., and Mesirov, J.P. (2005). Gene set enrichment analysis: a knowledge-based approach for interpreting genome-wide expression profiles. Proc. Natl. Acad. Sci. USA 102, 15545-15550. https://doi.org/10.1073/pnas.0506580102.

Surh, C.D., and Sprent, J. (1994). T-cell apoptosis detected in situ during positive and negative selection in the thymus. Nature 372, 100-103. https://doi. org/10.1038/372100a0.

Tonelli, C., Chio, I.I.C., and Tuveson, D.A. (2018). Transcriptional regulation by Nrf2. Antioxid. Redox Signal. 29, 1727-1745. https://doi.org/10.1089/ars.

Trzeciak, A., Wang, Y.-T., and Perry, J.S.A. (2021). First we eat, then we do everything else; the dynamic metabolic regulation of efferocytosis. Cell Metab. 33, 2126-2141. https://doi.org/10.1016/j.cmet.2021.08.001.

Vitale, I., Manic, G., Coussens, L.M., Kroemer, G., and Galluzzi, L. (2019). Macrophages and metabolism in the tumor microenvironment. Cell Metab. 30, 36-50. https://doi.org/10.1016/j.cmet.2019.06.001.

Wang, Y., Szretter, K.J., Vermi, W., Gilfillan, S., Rossini, C., Cella, M., Barrow, A.D., Diamond, M.S., and Colonna, M. (2012). IL-34 is a tissue-restricted ligand of CSF1R required for the development of Langerhans cells and microglia. Nat. Immunol. 13, 753-760. https://doi.org/10.1038/ni.2360.

Wang, Y.-P., and Lei, Q.-Y. (2018). Metabolite sensing and signaling in cell metabolism. Signal Transduct. Targeted Ther. 3, 30. https://doi.org/10.1038/ s41392-018-0024-7.

Wang, Z., Ying, Z., Bosy-Westphal, A., Zhang, J., Schautz, B., Later, W., Heymsfield, S.B., and Müller, M.J. (2010). Specific metabolic rates of major organs and tissues across adulthood: evaluation by mechanistic model of resting energy expenditure. Am. J. Clin. Nutr. 92, 1369-1377. https://doi.org/ 10.3945/ajcn.2010.29885.

Yates, A.J. (2014). Theories and quantification of thymic selection. Front. Immunol. 5, 13. https://doi.org/10.3389/fimmu.2014.00013.

Yurdagul, A., Jr., Subramanian, M., Wang, X., Crown, S.B., Ilkayeva, O.R., Darville, L., Kolluru, G.K., Rymond, C.C., Gerlach, B.D., Zheng, Z., et al. (2020). Macrophage metabolism of apoptotic cell-derived arginine promotes continual efferocytosis and resolution of injury. Cell Metab. 31, 518-533.e10. https://doi.org/10.1016/j.cmet.2020.01.001.

Zago, G., Saavedra, P.H.V., Keshari, K.R., and Perry, J.S.A. (2021). Immunometabolism of tissue-resident macrophages - an appraisal of the current knowledge and cutting-edge methods and Technologies. Front. Immunol. 12, 665782. https://doi.org/10.3389/fimmu.2021.665782.

Zagórska, A., Través, P.G., Lew, E.D., Dransfield, I., and Lemke, G. (2014). Diversification of TAM receptor tyrosine kinase function. Nat. Immunol. 15, 920-928. https://doi.org/10.1038/ni.2986.

Zenewicz, L.A. (2017). Oxygen levels and immunological studies. Front. Immunol. 8, 324. https://doi.org/10.3389/fimmu.2017.00324.

Zhang, S., Weinberg, S., DeBerge, M., Gainullina, A., Schipma, M., Kinchen, J.M., Ben-Sahra, I., Gius, D.R., Yvan-Charvet, L., Chandel, N.S., et al. (2019). Efferocytosis fuels requirements of fatty acid oxidation and the electron transport chain to Polarize macrophages for tissue repair. Cell Metab. 29, 443-456.e5. https://doi.org/10.1016/j.cmet.2018.12.004.

Zhou, T., Hsu, H., Tu, Y., Lin, C., Chen, N., Tsai, J., and Robey, E.A. (2021). Thymic macrophages consist of two populations with distinct localization and origin. Preprint at biorxiv. https://doi.org/10.1101/2021.11.04.

## **Cell Reports Article**



### **STAR**\***METHODS**

### **KEY RESOURCES TABLE**

REAGENT or RESOURCE	SOURCE	IDENTIFIER
Antibodies		
Anti-CD64 Alexa Fluor 647 (clone: X54-5/7.1)	BioLegend	Cat#139322; RRID:AB_2566561
Anti-CD11b FITC (clone: M1/70)	BioLegend	Cat#101205; RRID:AB_312788
Anti-F4/80 PE (clone: BM8)	BioLegend	Cat#123110; RRID:AB_893486
Anti-CD64 APC (clone: X54-5/7.1)	BioLegend	Cat#139306; RRID:AB_11219391
Anti-CD64 FITC (clone: AT152-9)	Bio-Rad	Cat#MCA5997; RRID:AB_2687456
Anti-CD11b Brilliant Violet 785 (clone: M1/70)	BioLegend	Cat#101243; RRID:AB_312788
Anti-CD11b PE (clone: M1/70)	BioLegend	Cat#101207; RRID:AB_312790
Anti-F4/80 Brilliant Violet 421 (clone: BM8)	BioLegend	Cat#123137; RRID:AB_2563102
Rat anti-MerTK (clone: DS5MMER)	Thermo Fisher Scientific	Cat#14-5751-82; RRID:AB_2688282
Rabbit anti-HIF-1α (clone: D1S7W)	Cell Signaling Technology	Cat#36169; RRID:AB_2799095
Goat anti-rat IgG Alexa Fluor 647	Thermo Fisher Scientific	Cat#A-21247; RRID:AB_141778
Goat anti-rabbit IgG Alexa Fluor 488	Thermo Fisher Scientific	Cat#A-11008; RRID:AB_143165
Rabbit anti-NRF2 (clone: D1Z9C)	Cell Signaling Technology	Cat#12721; RRID:AB_2715528
Donkey anti-rabbit IgG PE	Jackson ImmunoResearch Labs	Cat#711-116-152; RRID:AB_2340599
Rabbit anti-LC3B (clone: E7X4S)	Cell Signaling Technology	Cat#43566; RRID:AB_2910544
Chemicals, peptides, and recombinant protein	S	
Phorbol 12-myristate 13-acetate (PMA)	Sigma-Aldrich	Cat#P8139
Collagenase P	Roche	Cat#11213865001
DNase I	Roche	Cat#10104159001
Propidium iodide	Sigma-Aldrich	Cat#P4864
DAPI	BioLegend	Cat#422801
Dexamethasone	Sigma-Aldrich	Cat#D4902
2-NBDG	Thermo Fisher Scientific	Cat#N13195
<sup>13</sup> C <sub>6</sub> -glucose	Sigma-Aldrich	Cat#389374
6-aminonicotinamide	Cayman Chemical	Cat#10009315
N-acetylcysteine	Sigma-Aldrich	Cat#A9165
Glutathione reduced ethyl ester	Sigma-Aldrich	Cat#G1404
Critical commercial assays		
Percoll Plus	GE	Cat#17-5445-01
CellROX Green	Thermo Fisher Scientific	Cat#C10444
CellROX Deep Red	Thermo Fisher Scientific	Cat#C10422
TaqMan Universal Master Mix II, with UNG	Thermo Fisher Scientific	Cat#4440038
iQ SYBR Green Supermix	Bio-Rad	Cat#1708880
Zombie Aqua Fixable Viability Kit	BioLegend	Cat#423101
Chromium Single Cell 3' Reagent Kits	10X Genomics	Cat#PN-1000092
GSH/GSSG-Glo Assay	Promega	Cat#V6611
NADP/NADPH Quantification Colorimetric kit	BioVision	Cat#K347-100
Lipofectamine 2000 Transfection Reagent	Thermo Fisher Scientific	Cat#11668019
pHrodo Red	Thermo Fisher Scientific	Cat#P36600
Total Polyamine Assay Kit	Abcam	Cat#ab239728
Membrane Fluidity Kit	Abcam	Cat#ab789819
Alexa Fluor 488 Phalloidin	Thermo Fisher Scientific	Cat#A12379
Click-iT Plus TUNEL Assay	Thermo Fisher Scientific	Cat#C10619

(Continued on next page)





Continued		
REAGENT or RESOURCE	SOURCE	IDENTIFIER
Deposited data		
RNA sequencing data	This paper	GEO: GSE203543
Single-cell RNA sequencing data	This paper	GEO: GSE185460
ImmGen RNA sequencing of macrophages	(Heng and Painter, 2008), (Aguilar et al., 2020)	GEO: GSE122108
Metabolomics analysis of thymic macrophage and peritoneal macrophage	This paper	Metabolomic Workbench: ST002177
Code	This paper	Zenodo: 6588586
Experimental models: Cell lines		
THP-1	ATCC	RRID:CVCL_0006
Experimental models: Organisms/strains		
C57BL/6	The Jackson Laboratory	RRID:IMSR_JAX:000664
Macrophage Fas-induced Apoptosis (MaFIA) C57BL/6	The Jackson Laboratory	Stock No: 005070; RRID:IMSR_JAX:005070
ROSA26 <sup>GFP</sup>	Dzhagalov Laboratory	N/A
Oligonucleotides		
Primers (See Table S1)	This paper	N/A
siRNAs (See Table S1)	This paper	N/A
Software and algorithms		
Zen 2012 blue edition (1.1.2.0)	Zeiss	http://www.zeiss.com/microscopy/en_us/products/ microscope-software/zen.html#introduction; RRID:SCR 013672
Imaris Cell Imaging Software	Oxford Instruments	http://www.bitplane.com/imaris/imaris; RRID:SCR_007370
Progenesis QI	Waters	http://www.nonlinear.com/progenesis/qi-for-proteomics; RRID:SCR_018923
MetaboAnalyst 5.0	(Chong et al., 2019)	https://www.metaboanalyst.ca/; RRID:SCR_015539
Gene Set Enrichment Analysis (4.3.0)	(Subramanian et al., 2005), (Mootha et al., 2003)	https://www.gsea-msigdb.org; RRID:SCR_003199
Shiny GAM: integrated analysis of genes and metabolites	(Sergushichev et al., 2016)	https://artyomovlab.wustl.edu/shiny/gam
Cytoscape (3.7.2)	(Shannon et al., 2003)	https://cytoscape.org; RRID:SCR_003032
Cell Ranger	10X Genomics	https://support.10xgenomics.com/single-cell-gene- expression/software/pipelines/latest/what-is-cell- ranger; RRID:SCR_017344
Loupe Browser	10X Genomics	https://support.10xgenomics.com/single-cell-gene- expression/software/visualization/latest/what-is-loupe- cell-browser; RRID:SCR_018555
MassHunter Profinder Software	Agilent	https://www.agilent.com/en/product/software-informatics/mass-spectrometry-software/data-analysis/qualitative-analysis; RRID:SCR_019081
Graph Pad Prism 6	GraphPad	http://www.graphpad.com; RRID:SCR_002798
FlowJo (V10)	BD	https://www.flowjo.com/solutions/flowjo; RRID:SCR_008520
BioRender	BioRender	http://biorender.com; RRID:SCR_018361

### **RESOURCE AVAILABILITY**

### **Lead contact**

Further information and requests for resources and reagents should be directed to and will be fulfilled by the lead contact, Chia-Lin Hsu (clhsu@nycu.edu.tw).

### **Materials availability**

This study did not generate new unique reagents.



#### Data and code availability

- RNAseq data have been deposited at GEO and the metabolomics data have been deposited at Metabolomics Workbench. The data are publicly available as of the date of publication. Accession numbers are listed in the key resources table.
- All original code has been deposited at Zenodo and is publicly available as of the date of publication. Accession ID is listed in the key resources table.
- Any additional information required to reanalyze the data reported in this paper is available from the lead contact upon request.

### **EXPERIMENTAL MODEL AND SUBJECT DETAILS**

C57BL/6 mice were purchased from the National Laboratory Animal Center, Taiwan. The Macrophage Fas-induced Apoptosis (MaFIA) mice were obtained from The Jackson Laboratory (Stock No: 005070) (Burnett et al., 2004). ROSA26GFP were generated at the Dzhagalov lab. All mice were bred and maintained in the specific-pathogen-free room at NYCU Animal Center. Equal ratios of male and female mice age between 4-8 weeks were used in the study. All experimental procedures were approved and performed according to the NYCU Institutional Animal Care and Use Committee guidelines.

#### **METHOD DETAILS**

#### **Bone marrow-derived macrophages**

Total bone marrow cells were harvested from 5-8 weeks old C57BL mice. The total bone marrow single cell suspension was prepared, red blood cells removed and cultured in complete DMEM (DMEM supplemented with 2 mM L-glutamine, 1 mM sodium pyruvate, 100 U/mL penicillin/streptomycin, non-essential amino acids, and 10% heat-inactivated fetal bovine serum) and L929 conditional media at 37°C with 5% CO2 for 6 days. The medium was refreshed every 3 days. At end of the culture, the medium was replaced with a complete DMEM and considered BMDMs for further experiments.

### **THP-1** derived macrophage

The THP-1 cell line was routinely maintained in complete RPMI (RMPI 1640 supplemented with 2 mM L-glutamine, 1 mM sodium pyruvate, 100 U/mL penicillin/streptomycin, non-essential amino acids, and 10% heat-inactivated fetal bovine serum). To induce the macrophage differentiation, THP-1 cells (106 cell/mL) were treated with 50 nM Phorbol 12-myristate 13-acetate (PMA) for 2 h, washed, and allowed additional differentiation for 16 h in culture. The resulting cells were considered THP-1-derived macrophages and subjected to further experiments.

### **Tissue-resident macrophage preparation**

To obtain the resident thymic macrophages, the thymus was harvested from 5 to 8 weeks old C57BL mice, cut into small pieces, and incubated in DMEM containing 0.4 mg/mL collagenase P and 0.4 mg/mL DNase I at 37°C for 20 min with frequent gentle mixing. The resulting cell suspension was overlaid on the 57% Percoll Plus solution at the volume ratio of 1:1 and centrifuged at 650 x g for 20 min at 4°C. The cells at the interface were collected and washed with PBS, and re-suspended in 24G2 supernatant at room temperature for 15 min for blocking. The anti-CD64, anti-CD11b, and anti-F4/80 antibody cocktail in FACS buffer (PBS with 0.5% bovine serum albumin (BSA) and 2 mM EDTA) was added to the sample and allowed incubation on ice for 20 min. At the end of the staining, the cells were centrifuged, washed, and re-suspended in propidium iodide containing FACS buffer. Live singlets with CD64+CD11bloF4/80+ were defined as resident thymic macrophages (TMφs) and sorted by BD FACSMelody with the purity > 95%. The peritoneal cavity macrophages (PCMφs) were collected by intra-peritoneal injected 5 mL of ice-cold complete DMEM, thoroughly rinsed the peritoneal cavity, and re-collected the solution containing the exudate cells. The cells were processed and stained as described above, and the CD11b<sup>+</sup>F4/80<sup>+</sup> cells were identified as PCMφs and harvested.

### Immunofluorescence staining

The thymus of 5–8 weeks old C57BL mice was harvested and fixed in PBS containing 4% paraformaldehyde at room temperature for 1 h. The thymus was then dehydrated with 30% sucrose in PBS at 4°C overnight, and subjected to OCT embedding. The resulting tissue blocks were stored at -80°C until use. The thymic slices at 20 μm were prepared and blocked with 5% goat serum in immunohistochemistry (IHC) buffer (0.1M Tris-HCl solution (pH = 7.4), with 0.5% BSA and 2% Triton X-100), at room temperature for 2 h. The slides were stained with the primary antibodies, anti-MerTK and anti-HIF-1α diluted in the blocking buffer at 4°C overnight. At end of the incubation, the slides were washed twice with 0.1M Tris-HCl buffer, and further incubated with secondary antibodies, goat antirat AF647 and goat anti-rabbit AF488, diluted in the IHC buffer at 4°C for 4 h. Following the Tris-HCl buffer wash, the slides were then stained with DAPI in IHC buffer at room temperature for 15 min. The images were captured with a Zeiss Axio Observer along with a Zeiss Apotome addition. The images were analyzed using the Zeiss Zen 2012 software and the 3D reconstruction was made using Imaris software.





#### Reactive oxygen species measurement

The ROS measurement was performed as described previously (Fan et al., 2021). In brief, the level of cellular reactive oxygen species was quantified by staining the cells with CellROX green or CellROX deep red in warm serum-free DMEM at 37°C for 30 min. After terminating the reaction by adding ice-cold PBS, the stained cells were co-stained with DAPI or propidium iodide and analyzed with BD LSRFortessa immediately.

#### **RNA extraction and Quantitative RT-PCR**

The RNA of the cells was extracted using TRI reagent according to the manufacturer's manual. The reverse transcription was performed by SuperScript III Reverse Transcriptase with oligo dT primer, in the presence of RNaseOUT reagent following the manufacturer's instructions. Quantitative PCR was performed on StepOnePlus Real-Time PCR system with TagMan universal master mix and TagMan expression assay probes (see table) or iQ SYBR Green Supermix following the manufacturer's manuals. The relative mRNA expression level was calculated by normalizing to the expression level of murine Rpl19 or human GAPDH and presented in the  $2^{-\Delta CT}$ or  $2^{-\Delta\Delta CT}$  format.

### Intracellular staining for flow cytometric analysis

The cells were blocked and surface stained as described in the tissue-resident macrophage preparation section. At the end of the staining, the cells were washed with ice-cold PBS and further stained with Zombie Aqua in PBS at room temperature for 20 min. The cells were then fixed with 4% paraformaldehyde and permeablized by adding Methanol at the volume ratio of 9:1 and incubated on ice for 20 min. After washing the cells with ice-cold PBS, the cells were stained with the primary antibodies in 24G2 supernatant at room temperature for 30 min, the procedure was repeated for the staining of secondary antibodies. The primary antibodies were anti-NRF2 or anti-HIF-1α; the secondary antibody was anti-rabbit IgG PE. Samples were collected with BD LSRFortessa and analyzed with FlowJo.

### Metabolomics of tissue-resident macrophages

Sorted 5 x 10<sup>5</sup> tissue-resident macrophages were re-suspended in 1 mL LC-MS grade methanol and processed to obtain the metabolites. In brief, the proteins in the sample were precipitated and removed while the supernatant was collected and evaporated by a vacuum concentrator. The resulting metabolite extracts were resolved in 50 μL of ultra-pure water and transferred to a reduced-volume autosampler vial for LC-MS analysis. For liquid chromatography, the ACQUITY BEH C18 column (100 mm length x 2.1 mm internal diameter, 1.7 μm particles) was used and maintained at 40°C in the ultra-performance liquid chromatography (UPLC). Samples were eluted with gradient process at 0.3 mL/min using mobile phase (A) 0.1% ammonium hydroxide in LC-MS grade water and mobile phase (B) 0.1% ammonium hydroxide in LC-MS grade acetonitrile (1% B for 0.5 min, 1-100% B in 4 min, 100% B for 0.5 min, 100-1% B in 1 min, 1% B for 3 min). The mass spectrometry data were acquired through the Waters Xevo G2-XS QTof in negative mode and processed by Progenesis QI software. The features were matched to the KEGG compounds through Chemspider while the mass error was limited to 15 ppm. This data is available at the NIH Common Fund's National Metabolomics Data Repository (NMDR) website, the Metabolomics Workbench, https://www.metabolomicsworkbench.org where it has been assigned Project ID: ST002177. The data can be accessed directly via it's Project DOI: https://dx.doi.org/10.21228/M8PT3H. This work is supported by NIH grant U2C-DK119886.

### Metabolomics pathway enrichment

Metabolomics data collected from the tissue-resident macrophages and apoptotic cell-treated BMDMs were subjected to MetaboAnalyst 5.0 for Mus musculus KEGG "pathway enrichment" analysis under "Fisher's Exact Test" mode. Metabolites with fold change >3 in TMφs compared with PCMφ or fold change >1.5 in treated BMDMs compared with the untreated were selected. An additional p < 0.05 threshold was set for all analyses. The results were plotted using the R package ggplot2.

### Gene set enrichment analysis

The RNA sequencing data of the BMDMs were acquired as described in the RNA sequencing section. After the differential gene expression analysis by the R package DESeq2 (1.30.0), datasets were analyzed following the GSEA software (4.0.3) under KEGG pathways or metabolic pathways.

### **Combined pathway enrichment analysis**

RNA sequencing data of the TMos and PCMos were extracted from the ImmGen database (GSE122108), gene annotation, and RPKM calculations were done following the ImmGen pipeline. Genes with expression level >3 fold and compounds that are >1.5 fold in TMφs compared with PCMφs were chosen for further analysis. To achieve metabolic pathway enrichment of TMφs, KEGG Mus musculus pathways were extracted through the R package KEGGREST (1.30.0). The chosen genes and compounds were limited to the genes and compounds of the KEGG metabolic pathways. Fisher's exact test was performed in greater mode with R package stats (4.0.3). The visualization of the metabolic network was done with GAM in the Cytoscape (3.7.2) environment.



### Single-cell RNA sequencing

The thymus of the MaFIA mice was harvested and enriched with myeloid cells by using 57% Percoll Plus solution as described in the earlier section. Instead of surface staining, GFP+ cells were sorted by using BD FACSMelody with purity >95% and viability >80%. The cells were spun down, re-suspended in PBS with 0.04% BSA, and subjected to library preparation. The single-cell RNA sequencing cell encapsulation and library preparation were done with the 10x Chromium Controller, Chromium Single Cell 3' Library, and Gel Bead Kit v3 following the manufacturer's recommendations. The libraries were sequenced on the NovaSeq 6000 system. Post-processing and quality control were performed by the NYCU Genome Center using the Cell Ranger package. Reads were aligned to mm10 reference assembly. Primary assessment for the MaFIA sample reported: 9,973 cell barcodes with 11,385 median unique molecular identifiers (UMIs, transcripts) per cell and 3,076 median genes per cell sequenced to 71.0% sequencing saturation with 94,260 mean reads per cell. The visualization of the cell populations and gene expression was done by Loupe Browser.

### **Apoptotic thymocytes preparation and treatment to BMDMs**

The thymus of C57BL mice was harvested and homogenized. The thymocytes were then treated with 10  $\mu$ M dexamethasone in complete DMEM at 37°C with 5% CO<sub>2</sub> for 6.5 h. The apoptosis induction was terminated by removing the dexamethasone-containing medium and replacing with fresh complete DMEM. The resulting apoptotic thymocytes were added to the BMDMs or THP-1 derived macrophages at a 40:1 ratio for 24 h as the efferocytosis treatment.

### **RNA** sequencing of **BMDMs**

The BMDMs were co-cultured with or without apoptotic thymocytes for 24 h and harvested for the RNA extraction as described earlier. The RNA concentration was measured by using a Qubit fluorometer with a Quant-iT RNA BR assay kit, and the RNA guality was examined on the Agilent Technologies 2100 Bioanalyzer with RNA nanochip. The library was prepared by using Illumina TruSeq Stranded mRNA Sample Prep Kit and sequenced by Illumina NextSeq High Output Kit v2.5-75 cycles on the NextSeq 550 platform. The raw data were aligned and analyzed following the CLC Genomics Workbench 20.0.4 pipeline. The sequence was annotated according to Mus musculus GRCm38 mm10. The differential gene expression analysis was calculated by using the R package DESeq2 (1.30.0).

### **GSH/GSSG** detection

The reduced and oxidized form of glutathione was detected using the GSH/GSSG-Glo Assay kit, which is a luminescent-based assay to quantify the GSH/GSSG ratios. In brief, cells were harvested and lysed on a white flat 96-well plate and measured for the reduced and oxidized glutathione concentration following the manufacturer's manual. The luminescence results were collected on Infinite 200 PRO reader.

### **NADP/NADPH** detection

NADP/NADPH Quantification Colorimetric kit was used to determine the intracellular NADP/NADPH levels. Following the manufacturer's manual, the samples were harvested and lysed on a flat 96-well plate and the results were collected by measuring the 450 nm absorbance with a TECAN Sunrise ELISA Reader.

### 2-NBDG uptake assay

BMDMs were treated with or without apoptotic thymocytes for 24 h. At the end of treatment, the BMDMs were treated with 10 µg/mL of 2-NBDG in complete RPMI 1640 and incubated at 37°C for 40 min. The reaction was terminated by removing the 2-NBDG containing medium and washing the BMDMs with ice-cold PBS. The samples were collected by BD LSRFortessa and analyzed by FlowJo.

### <sup>13</sup>C<sub>6</sub>-glucose tracing

After the BMDMs were co-cultured with apoptotic thymocytes for 24 h, non-phagocytosed cells were removed by PBS rinse, and the BMDMs were pulsed with 25 mM <sup>13</sup>C<sub>6</sub>-Glucose containing complete DMEM (glucose-free DMEM supplemented with 2 mM of L-glutamine, 1 mM of sodium pyruvate, 100 U/mL of penicillin/streptomycin, non-essential amino acids, and 10% heat-inactivated and dialyzed fetal bovine serum) for 2 h. The analytical parameters were based on (Jin et al., 2019) and modified. In brief, the metabolites were extracted after collecting the cells by adding 4:4:2 acetonitrile/methanol/ultra-pure water solution and sonicated for 5 min. The solution was centrifuged at 12,000 x g at 4°C for 10 min to remove cell particulates. The supernatant was transferred to a reduced-volume autosampler vial for LC-MS analysis. The samples were analyzed on an Agilent 1290 II Infinity Ultra-High-Performance Liquid Chromatography system with an Agilent Accurate Mass 6545XT-QTOF mass spectrometer. The column was a Waters Acquity UPLC BEH Amide (100 mm length X 2.1 mm internal diameter, 1.7 μm particles) maintained at 40°C. The mobile phase consisted of 15 mM ammonium acetate and 0.3% ammonium hydroxide (pH 9.5) in LC-MS grade water (mobile phase A) and 15 mM ammonium acetate and 0.3% ammonium hydroxide (pH 9.5) in LC-MS grade 90% acetonitrile (v/v) (mobile phase B). The flow rate was 0.3 mL min<sup>-1</sup>. The gradient profile: 10% B to 50% B in 8 min, 50% B held for 2 min, and the post time was 10 min. The mass spectrometer was equipped with an Agilent Jet-stream source operating in negative and positive ion mode with source parameters set as follows: Nebulizer gas, 45psi; Sheath gas temperature, 325°C. The resulting data were processed





using Agilent MassHunter Profinder software with an in-house targeted metabolite database created by Agilent Personal Compound Database and Library. The Profinder batch results were then corrected for <sup>13</sup>C natural abundance, and exported for statistical analysis.

### Inhibition of pentose phosphate pathway by 6-AN or siRNA

To inhibit the pentose phosphate pathway, 10 µM of 6-aminonicotinamide (6-AN) was added to the cells for 6 h to achieve the effect. To investigate the impact of PPP inhibition on BMDM phagocytosis, 6-AN was added to the culture during the last 6 h of apoptotic thymocyte co-culture treatment. The reaction was terminated by washing the BMDMs with warm PBS. The cells were subjected to phagocytosis assay or ROS measurement. For THP-1 cells, the inhibition of the pentose phosphate pathway was achieved by siRNA knockdown. G6PD Silencer Select siRNA or Silencer Select Negative Control No. 1 siRNA were introduced into the cells by Lipofectamine 2000) following the manufacturer's instructions. 6 h after the transfection, the supernatant was removed and replaced with complete RPMI for additional overnight culture. The resulting cells were further differentiated into macrophages and subjected to phagocytosis assay or ROS measurement.

### Phagocytosis assay

To test the ability of the macrophages to engulf apoptotic cells, the apoptotic thymocytes were prepared and labeled with pHrodo Red at room temperature for 30 min. The labeled apoptotic thymocytes were added to the macrophages at the ratio of 40:1 and allowed for efferocytosis at 37°C for 2 h. At end of the reaction, the macrophages were washed with PBS to remove residual cells, resuspended in DAPI containing FACS buffer, and subjected to flow cytometric analysis with BD LSRFortessa. The phagocytosis assay index was calculated as the mean fluorescent intensity (MFI) of the treated group minus the untreated MFI.

### Reactive oxygen species scavengers

To scavenge the reactive oxygen species induced by the efferocytosis, the ROS scavenging compound N-acetylcysteine (NAC, 1 mM) or glutathione reduced ethyl ester (GSH-MEE, 1 mM) was added together with the pHrodo-labeled apoptotic thymocytes to the THP-1 derived macrophages at 37°C for 2 h. After the reaction, the macrophages were washed with PBS and re-suspended in DAPI containing FACS buffer and subjected to flow cytometric analysis with BD LSRFortessa. The phagocytosis assay index was calculated as the mean fluorescent intensity (MFI) of the treated group minus the untreated MFI.

### **Treatment of thymus explants**

After carefully harvesting the thymus from the C57BL/6 or the B6-GFP mice, the two lobes of the thymus were separated and each injected with 20 µL of 10 µM 6-AN or solvent control (DMSO) in warm PBS by using a 29G syringe. The treated lobes were each placed in a 12-well plate well and covered with 10  $\mu$ M 6-AN or solvent control in complete DMEM. The treatment lasts for 6 h at 37°C with 5% CO2. The thymus was then shredded and digested for single-cell suspension, followed by the surface staining procedure. The oxidative stress of the cells was stained following the reactive oxygen species measurement procedure. The phagocytosis status of the macrophages was determined by GFP accumulation detection. The stained cells were co-stained with propidium iodide and analyzed with BD LSRFortessa.

### **Membrane fluidity measurement**

The membrane fluidity kit was used to measure the membrane fluidity of the cells following the manufacturers' instructions. In short, the treated BMDMs were measured with fluorescent emission at 400 nm and 470nm under 350 nm excitation after incubation with fluorescent lipid reagent and pluronic F127 solution. The relative membrane fluidity was calculated as a ratio of excimer 450 nm to monomer 400 nm. The fluorescence results were collected on Infinite 200 PRO reader.

### **Cytoskeleton dynamics**

To measure the cytoskeleton dynamics of the treated cells, the cells were stained with fluorescent-conjugated phalloidin for the F-actin detection. The staining was performed according to the manufacturer's instructions. In brief, the cells were fixed with 3.7% paraformaldehyde and pored with Triton X-100 before being stained with phalloidin. The stained cells were imaged using the Zeiss Axio Observer. The acquired images were then analyzed for F-actin signal using ImageJ.

### **Total polyamine measurement**

The polyamine level of the cells was measured by using the total polyamine assay kit. The treated cells were collected and measured with the polyamine level following the manufacturer's instructions. The lysate was measured with fluorescent at emission 587 nm under 535 nm excitation. The fluorescence results were collected on Infinite 200 PRO reader.

### **Dexamethasone-induced injury model**

To establish a dexamethasone-induced injury model, the 5 to 8 weeks old B6-GFP mice were intraperitoneally injected with 10 μg per g body weight of dexamethasone in PBS of the volume of 1% body weight. 6 h after the treatment, the thymus was harvested and proceed with the thymus explant treatment.

### **Cell Reports Article**



#### Intrathymic injection

To block the pentose phosphate pathway in vivo, the 4 to 6 weeks old B6 mice were anesthetized with isoflurane and intrathymically injected with 20 μM 6-AN along with 500x diluted Indian ink in 15 μL PBS. The injection sites locate beneath the first ribs and on both sides of the sternum. A BD 29G insulin syringe was used for the injection. The needle goes in the chest as deep as 4.53 mm. 6 h after injection, the mice were sacrificed and checked for Indian ink stain on both thymus lobes to assure successful injections, lobes with abnormal blood clot formation were excluded. The thymus was then harvested and stained with Annexin V according to the manufacturer's instructions. The suspended cells were analyzed by using BD LSRFortessa.

#### Apoptotic cell labeling in thymus

To label the apoptotic thymocytes in the thymus, the thymus slides were prepared as described in the earlier immunofluorescence staining section. After thymus slide preparation, the tissue slides were stained with TUNEL assay kit following the manufactorer's instruction. In short, the DNA break of the cells were incorporated with EdUTP by unsing the TdT enzyme. After the TUNEL staining process, the slides were stained with surface marker as described in the immunofluorescence staining section. The images were captured with a Zeiss Axio Observer along with a Zeiss Apotome addition. The images were analyzed using the Zeiss Zen 2012 software and the 3D reconstruction was made using Imaris software.

#### **QUANTIFICATION AND STATISTICAL ANALYSIS**

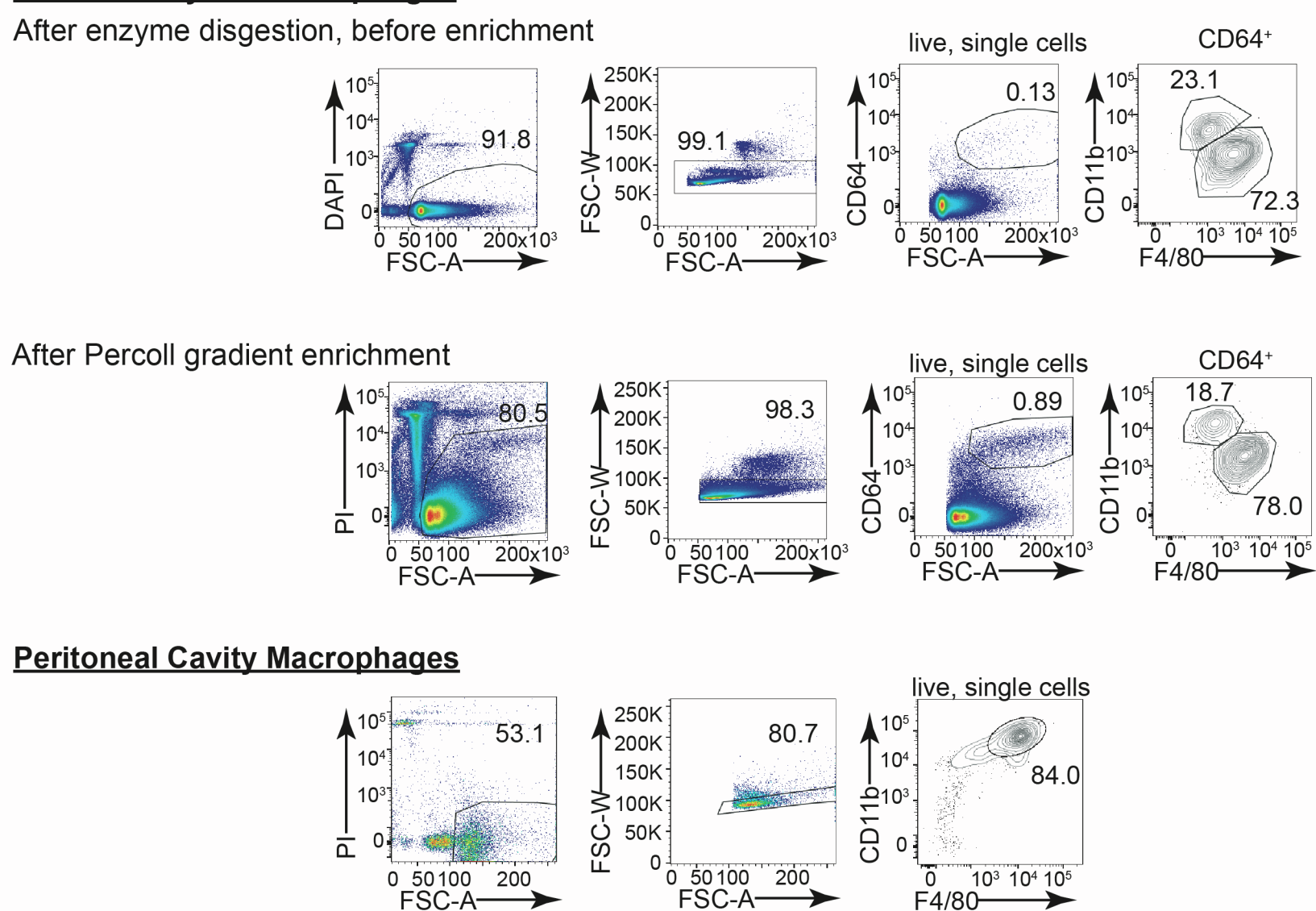
All statistics were performed using Graph Pad Prism 6. Statistical significance was calculated by Student's t-test when comparing two groups or one-way ANOVA when in comparison of multiple groups. For all the in vitro experiments, the n stands for biological repeats (eg. from pooled sorted primary cells). For the thymic explant or in vivo experiments, the n represents number of animals used. All error bars represent SEM with mean. All the statistics details can be found in the figure legends. Flow cytometry data were analyzed using FlowJo (V10). The graphic illustration was made with BioRender.

### **Supplemental information**

Multiomics reveal the central role of pentose phosphate pathway in resident thymic macrophages to cope with efferocytosis-associated stress

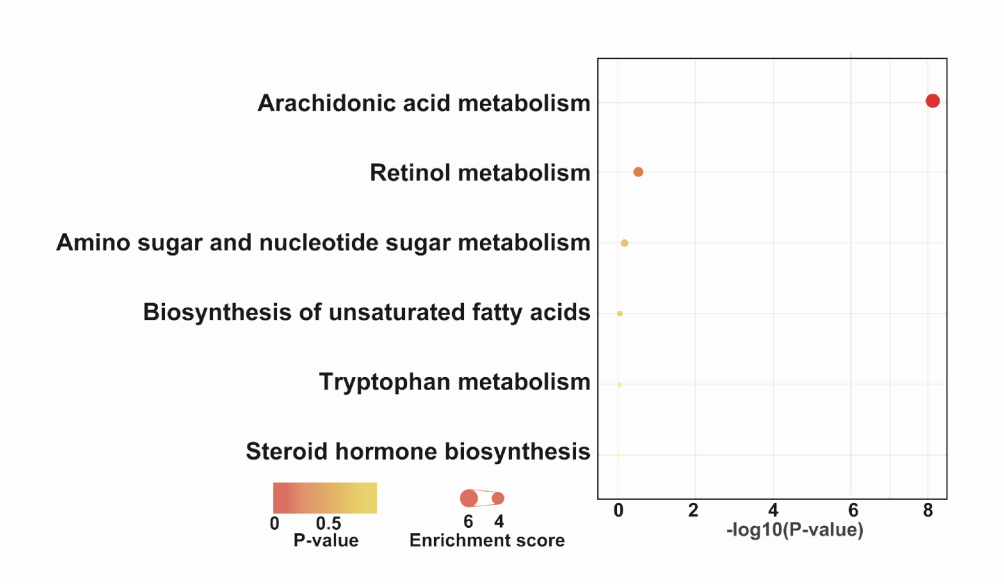
Tsung-Lin Tsai, Tyng-An Zhou, Yu-Ting Hsieh, Ju-Chu Wang, Hui-Kuei Cheng, Chen-Hua Huang, Pei-Yuan Tsai, Hsiu-Han Fan, Hsing-Kai Feng, Yu-Chia Huang, Chen-Ching Lin, Chao-Hsiung Lin, Chih-Yu Lin, Ivan L. Dzhagalov, and Chia-Lin Hsu

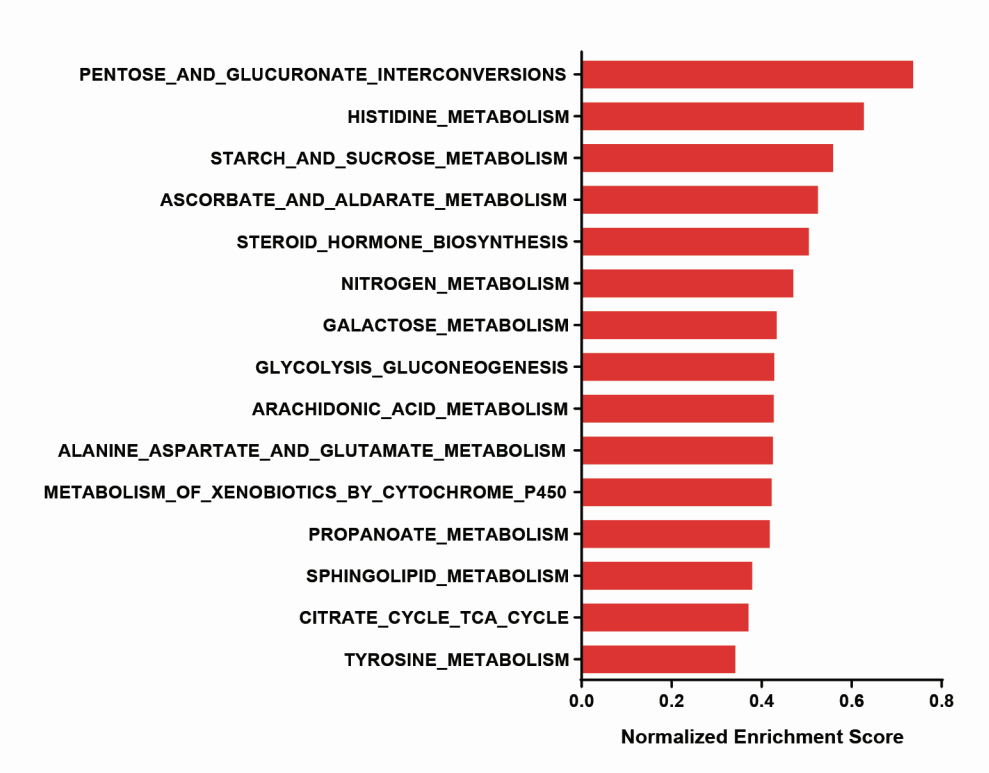
### **Resident Thymic Macrophages**



**Supplemental Figure 1.** Representative flow cytometric plots showing the gating strategy and enrichment of resident thymic macrophages (top) and peritoneal cavity macrophages (bottom). Related to Figure 1.

### **Supplemental Figure 2**

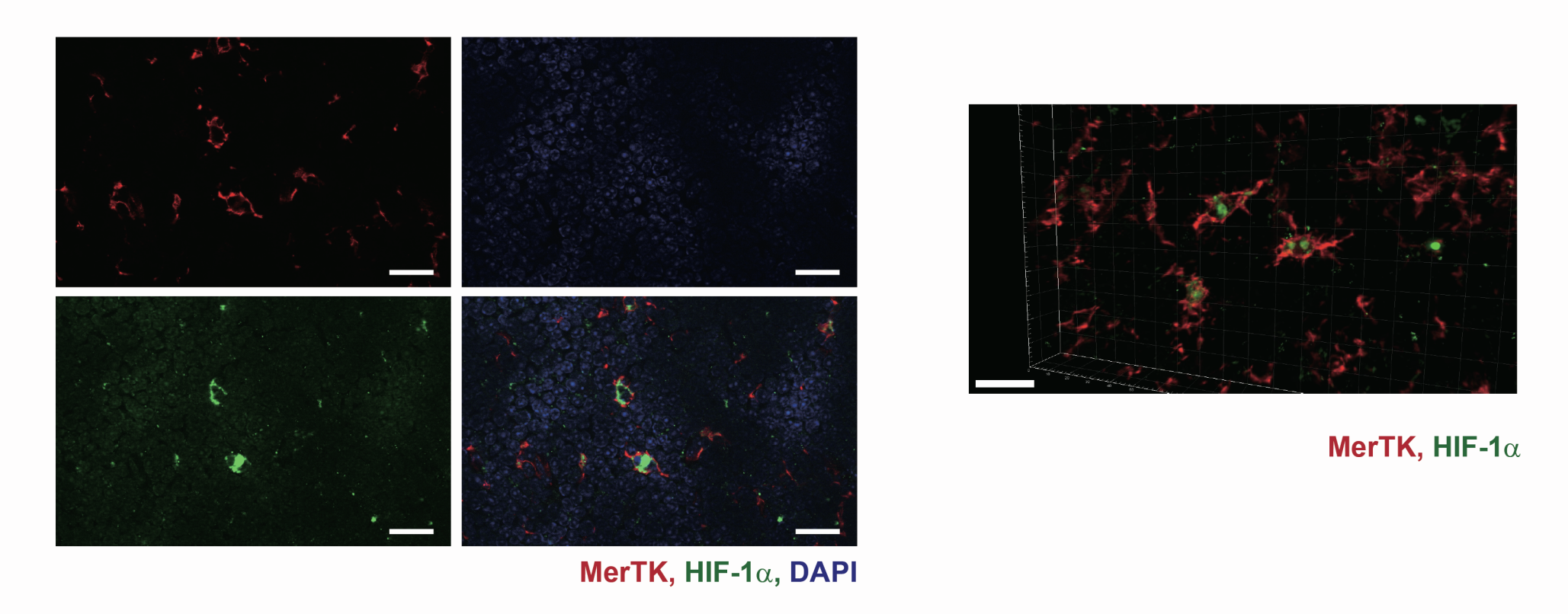




KEGG ID	Pathway	Match (%)	P-value
mmu00590	Arachidonic acid metabolism	25%	2.7E-06
mmu00830	Retinol metabolism	6%	4.6E-06

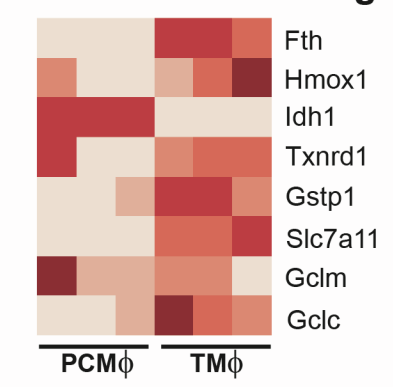
**Supplemental Figure 2.** Metabolomic and transcriptomic analyses highlighting the preferred metabolic pathways in peritoneal cavity macrophages. Related to Figure 1.

a b

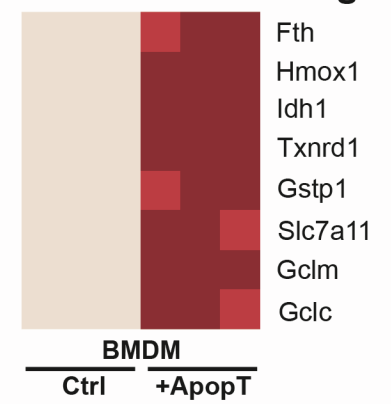


**Supplemental Figure 3.** (a) Immuno-stained thymic slices identify MerTK<sup>+</sup> macrophages have strong HIF-1 $\alpha$  accumulation. (b) A 3-D reconstruction of the images confirmed that although moderate HIF-1 $\alpha$  signals can be detected throughout the thymus, it is highly concentrated in the resident thymic macrophages. Scale bar =20  $\mu$ m. Related to Figure 2.

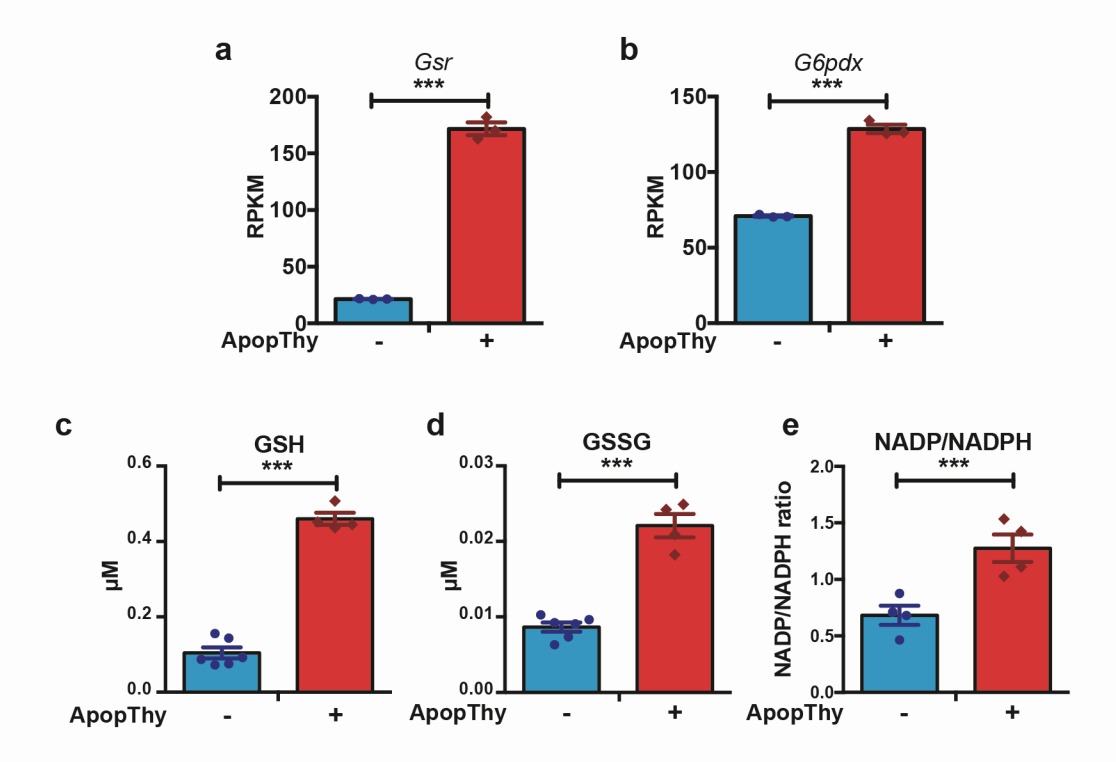
### a NRF2 downstream genes



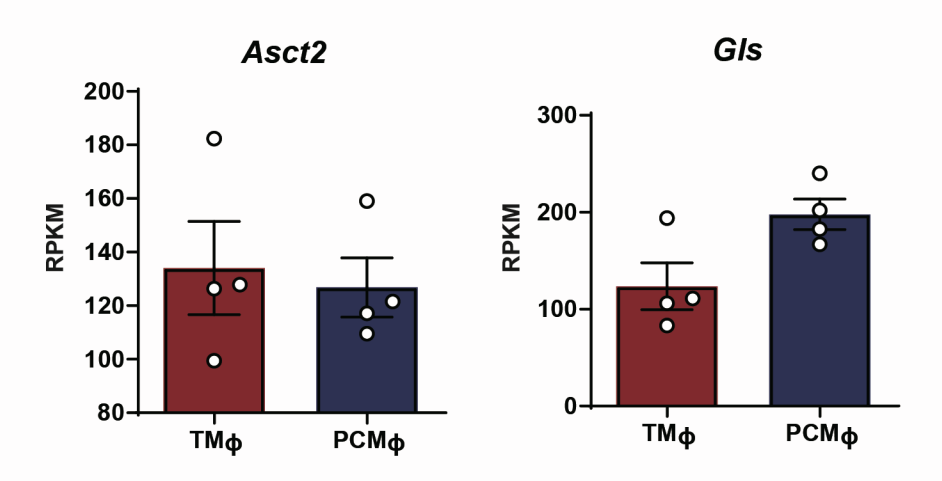
### b NRF2 downstream genes



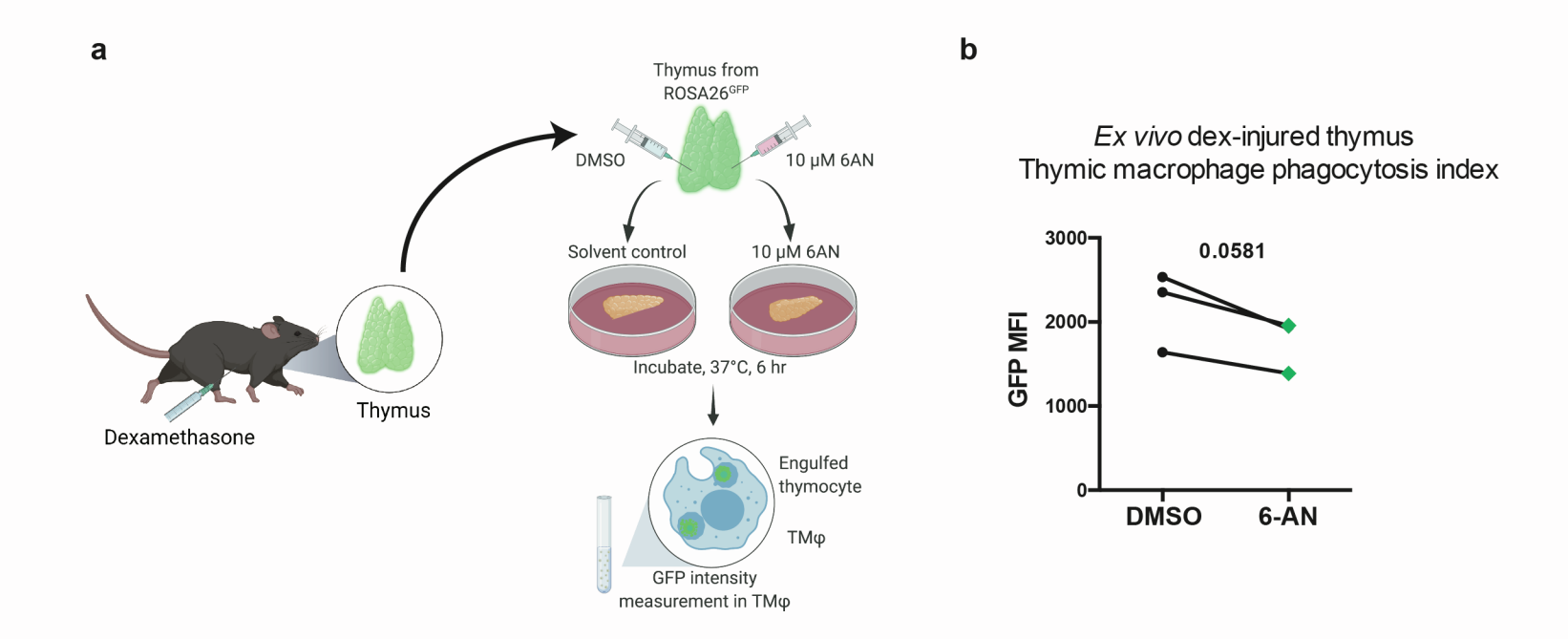
**Supplemental Figure 4.** Comparasion of selected NRF2 downstream gene expression in (a) *ex vivo* PCM<sub>Φ</sub> and TM<sub>Φ</sub> and (b) efferocytosing BMDM. Data extrapolated from RNAseq results of Fig. 1 and Fig 3, resepectively. Related to Figure 2 and 4.



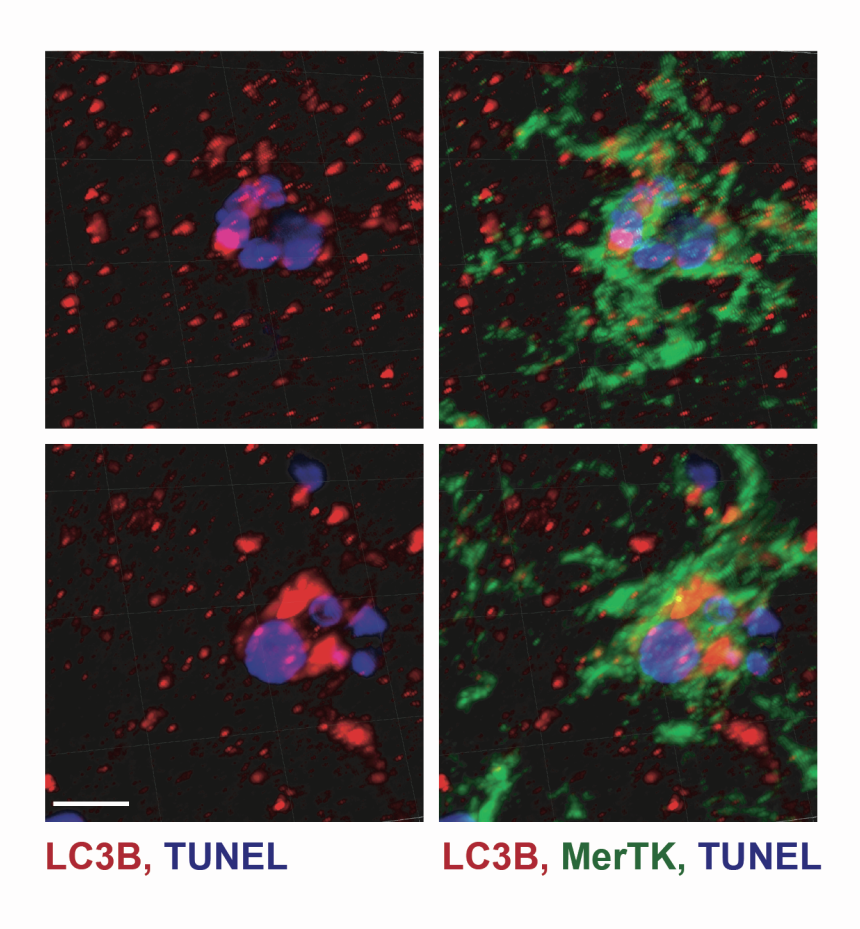
**Supplemental Figure 5.** Transcriptomic and functional analyses on BMDMs efferocytosed apoptotic thymocytes. Transcription of enzymes associated with PPP activity, *Gsr* (a) and *G6pdx* (b) were increased upon efferocytosis (n=3). The efferocytosis was also linked with higher redox demands as shown by elevation of GSH (c), GSSG (d), and NADP/NADPH (e) levels (n=4) by measured by luminescent-based and colorimetric assay, respectively. One-way ANOVA was used for statistical analysis, \*\*\* p < 0.001. Related to Flgure 3.



**Supplemental Figure 6.** Comparasion of the expression non-canonical glutaminolysis key factors, glutamine transporter, ASCT2, and the glutaminase-1 (GLS) in PCM $\phi$  and TM $\phi$  populations. Related to Figure 6.



**Supplemental Figure 7.** Functional PPP contributes to the efficient removal of apoptotic thymocytes in dexamethasone-induced thymus injury model. (a) illustration of experimental procedures. In brief, dexamethasone was i.p. administered into GPF mice for 16 hrs to induce the thymus injury. The thymus explants were then harvested and treated with 6-AN to block PPP. (b) The phagocytosis of apoptotic thymocytes was evaluated by the GFP intensity withinTMφs via FACS analysis. Related to Figure 7.



**Supplemental Figure 8.** Immuno-stained thymic slice shows that TMf can use LC3-associated phagocytosis to remove apoptotic thymocytes. Thymic slices were stained with LC3 to label the LC3-associated phagosomes, TUNEL to identify the apoptotic thymocytes, and MerTK to mark the TM $_{\phi}$ s. Shown were the close-up images of two representative TM $_{\phi}$ s. Scale bar = 5  $_{\mu}$ m. The 3D reconstruction images were made with Imaris. Related to Figure 2.

REAGENT or RESOURCE	SOURCE	IDENTIFIER		
Oligonucleotides				
TaqMan: Rpl19	Thermo Fisher Scientific	Assay ID:Mm02601633_g1; Cat#4331182		
TaqMan: Sirt2	Thermo Fisher Scientific	Assay ID:Mm01149204_m1; Cat#4331182		
TaqMan: Sirt3	Thermo Fisher Scientific	Assay ID:Mm00452131_m1; Cat#4331182		
TaqMan: <i>Hif1a</i>	Thermo Fisher Scientific	Assay ID:Mm00468869_m1; Cat#4331182		
TaqMan: Gsr	Thermo Fisher Scientific	Assay ID:Mm00439154_m1; Cat#4331182		
TaqMan: G6pdx	Thermo Fisher Scientific	Assay ID:Mm00656735_m1; Cat#4331182		
TaqMan: <i>Gclc</i>	Thermo Fisher Scientific	Assay ID:Mm00802658_m1; Cat#4331182		
TaqMan: <i>Nfe2l2</i>	Thermo Fisher Scientific	Assay ID:Mm00477784_m1; Cat#4331182		
Primer Human <i>G6PD</i> forward:	(Li et al., 2020)	N/A		
5'-CGAGGCCGTCACCAAGAAC-3'				
Primer Human <i>G6PD</i> reverse:	(Li et al., 2020)	N/A		
5'-GTAGTGGTCGATGCGGTAGA-3'				
Primer Human <i>GAPDH</i> forward:	(Hara et al., 2015)	N/A		
5'-GGAGTCCACTGGCGTCTTCA-3'				
Primer Human <i>GAPDH</i> reverse:	(Hara et al., 2015)	N/A		
5'-TGGTTCACACCCATGACGAA-3'				
Human G6PD Silencer Select siRNA	Thermo Fisher Scientific	Assay ID:s5447; Cat#4390824		
Silencer Select Negative Control No. 1 siRNA	Thermo Fisher Scientific	Cat#4390843		

Supplemental Table 1. Oligonucleotides used in this study.